The Observed Structure of Tropospheric Stationary Waves and the Local Balances of Vorticity and Heat[1]

NGAR-CHEUNG LAU[2]

Department of Atmospheric Sciences, University of Washington, Seattle 98195

(Manuscript received 3 November 1978, in final form 27 February 1979)

ABSTRACT

The physical structure and the associated transport properties of stationary waves in the troposphere are described using circulation statistics compiled from twice-daily hemispheric analyses covering 11 winters. The distributions of standing eddy meridional transports in middle latitudes are characterized by momentum flux convergence and equatorward geopotential energy transports in the upper troposphere, and by poleward heat fluxes at the lower levels.

The contributions of steady and transient motions to the local, time-averaged budget of vorticity at 300 mb are evaluated. The dominant terms in the time-averaged vorticity equation are the local advection of relative vorticity by the stationary flow and the divergence term. The advection of planetary vorticity by the mean flow (the β-effect) and the convergence of vorticity fluxes by transient eddies appear to be of secondary importance. The hemispheric distributions of the principal terms in the vorticity balance are closely related to topographical features at the lower boundary.

The hemispheric field of stationary flow divergence at various levels is determined as a residual in the time-averaged vorticity balance. This diagnosed divergence field is used to 1) demonstrate the feasibility of retrieving essential stationary flow features in the upper troposphere through solution of the linearized vorticity equation with a prescribed divergence forcing; 2) deduce the velocity potential field; and 3) compute the mean vertical motion field through vertical integration of the continuity equation.

Standing eddy statistics involving vertical motions are described. Mean vertical motions in middle latitudes are found to be positively correlated with mean meridional motions and with mean temperature. The distributions of meridional and vertical transports of geopotential energy and westerly momentum in the meridional plane are presented in a vectorial format. The pattern depicting geopotential energy fluxes suggests that the enhanced standing wave kinetic energy over the subtropics is maintained by geopotential energy transports which originate from higher latitudes.

A diagnosis of the local, time-averaged balance of heat at 1000 and 700 mb is performed. The heat transports by the transient eddies in the lower troposphere exhibit a strong tendency to destroy the zonally asymmetric component of the stationary temperature field. This dissipative mechanism acts on a time scale of several days. The hemispheric distributions of the diabatic heating deduced from the heat budget are indicative of the central role of geographically fixed influences such as ocean currents and sea-land contrast.

1. Introduction

The seasonally averaged circulation of the troposphere is characterized in middle latitudes by planetary scale wave motions which exist primarily as forced responses to inhomogeneities in the earth's topography and in the distribution of diabatic heating. The influence of large-scale orography on the atmospheric flow has been investigated by Charney and Eliassen (1949) and Bolin (1950) using barotropic models. Smagorinsky (1953) demonstrated that thermal forcing also plays an important role. More complicated tools have been used in subsequent studies to incorporate the composite effects of thermal and orographic forcing. These

include the quasi-geostrophic models of Saltzman (1965) and Derome and Wiin-Nielsen (1971), the two-layer, linearized primitive equation model of Egger (1976a,b), and the general circulation model experiments analyzed by Kasahara *et al.* (1973), Manabe and Terpstra (1974) and Hayashi and Golder (1977). These and other works suggest that both orography and diabatic heating are important in the maintenance of the stationary waves.

The structure and energetics of the stationary waves have also been investigated in many observational studies. The hemispheric distributions of the time-averaged wind, temperature and geopotential height fields have been documented by Crutcher (1959) and Crutcher and Meserve (1970). Van Loon *et al.* (1973) described the structure of the standing waves in terms of the amplitudes and phases of the first three zonal harmonic components. Statistics on the standing eddy

variances and covariances have been extensively documented by Oort and Rasmusson (1971). The energy conversions between the zonally averaged flow and various zonal harmonic components have been estimated by Saltzman and Fleisher (1960a,b) and Wiin-Nielsen et al. (1963, 1964). The hemispheric distribution of diabatic heating and its role in the generation of available potential energy have been examined by Brown (1964). These and other studies on large-scale atmospheric energetics in the wave-number domain have been summarized in a review by Saltzman (1970). The energy balance of the standing waves has also been examined by Holopainen (1970) for winter, summer and annual mean conditions over the Northern Hemisphere. This study indicates that the stationary waves are characterized by an energy cycle which is similar to that of baroclinic waves. The available potential energy of these waves is derived from the zonally averaged flow through down-gradient heat transports. It is then converted into kinetic energy to offset the dissipation due to friction and large-scale transient eddies.

The regional characteristics of the transient eddies embedded in the winter mean circulation have been described by Blackmon et al. (1977) and Lau (1978, 1979). It was noted in these studies that the properties of the transient waves at any given location are closely linked to the position of that site relative to the stationary wave features. The diagnoses of local, time-averaged budgets of momentum and kinetic energy by Lau (1978, 1979) further suggest that the stationary component of the circulation plays a dominant role in the local balances, whereas the effects of the transient eddies are seen to be of secondary importance. These results clearly indicate that a better understanding of the stationary wave structure and its maintenance is of primary concern in our effort to provide a comprehensive description of the general circulation. The objective of the present paper is to describe various observed characteristics of the stationary component of the Northern Hemisphere wintertime circulation. By making use of circulation statistics derived from twice-daily synoptic analyses, the three-dimensional structure of the observed stationary waves and the associated transport characteristics are documented. The hemispheric distributions of the time-averaged vertical motion and diabatic heating fields are then estimated by diagnosing the absolute vorticity and thermodynamic energy equations, respectively. The nature and relative importance of the stationary flow and transient eddies in the local vorticity and heat balances are evaluated by considering the individual terms in these budgets.

The present study makes use of the circulation statistics compiled from twice-daily National Meteorological Center (NMC) analyses of geopotential height, temperature and wind components at selected pressure levels. The analyses cover the 11 winters from 1965–66
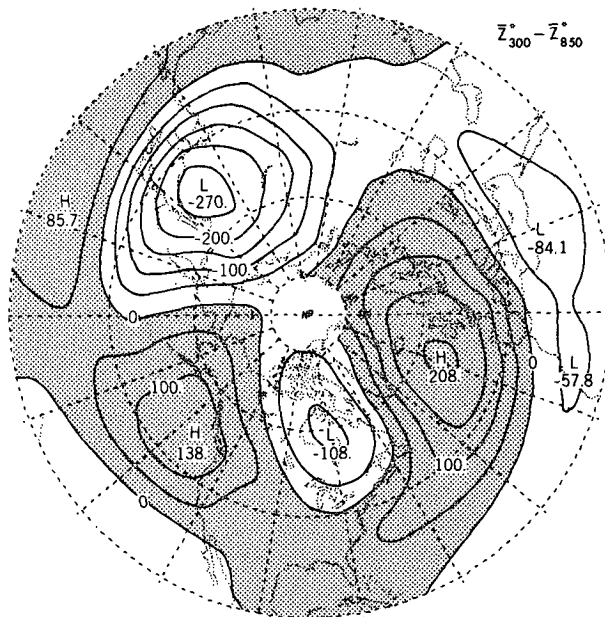

FIG. 1. Distribution of departure from zonal symmetry of the time averaged 850–300 mb thickness, $\bar{z}^*_{300 \, mb} - \bar{z}^*_{850 \, mb}$. Contour interval 50 m. In this and other figures displayed on polar stereographic projections, the meridians and latitude circles are drawn at intervals of 20°, with the outermost latitude circle representing 20°N.

through 1975–76. The winter season is taken to be the 120-day period starting from 15 November.

2. The three-dimensional structure of the stationary waves

The observed standing waves in the troposphere and lower stratosphere have been described by van Loon et al. (1973) in terms of the first three zonal harmonic wave components. In order to visualize more clearly how these perturbations are related to the underlying distribution of continents and oceans, the three-dimensional structure of these stationary perturbations may also be described by displaying the zonally asymmetric component of time-averaged fields in terms of hemispheric maps as well as longitude-height cross sections taken along selected latitude circles. In Fig. 1 is shown the distribution of the departures from zonal symmetry of the 11-winter average 850–300 mb thickness field. These stationary perturbations attain maximum amplitudes at about 50°N. The positive departures in the middle latitudes, which correspond approximately to the ridges in the stationary wave pattern, are located over the eastern oceans, whereas negative departures (troughs) are found over the eastern part of the two major land masses. Another prominent feature in Fig. 1 is the reversal in sign of the departures as one moves meridionally across the 30°N latitude circle.
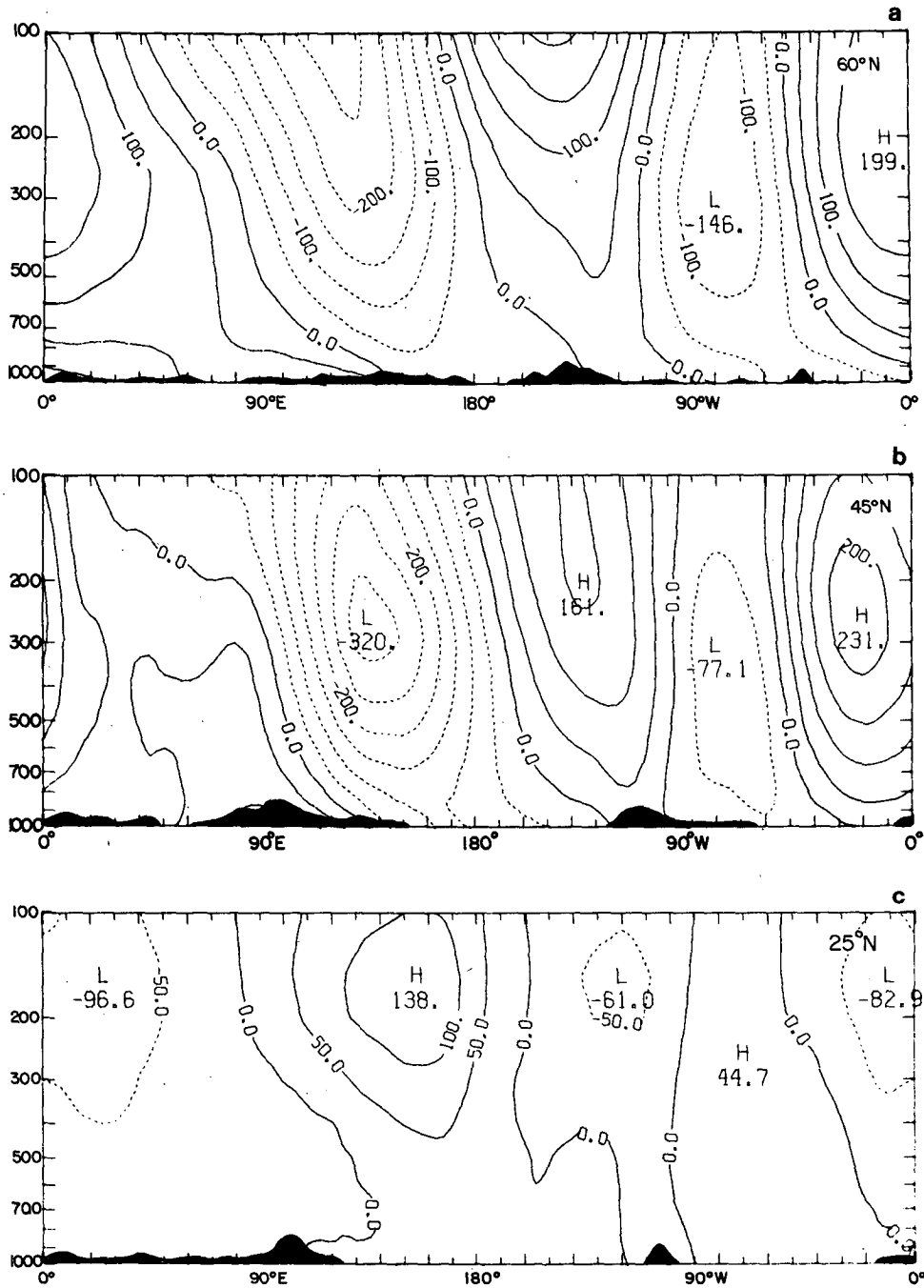
The departures from zonal symmetry of the time-

FIG. 2. Longitude-height cross sections of departure from zonal symmetry of the time-averaged geo-potential height field $\bar{z}^*$ taken along (a) 60°N, (b) 45°N and (c) 25°N latitude circles. Contour interval 50 m. The local orography is depicted at the bottom of the figures.

averaged geopotential height and temperature fields are shown in Figs. 2 and 3, respectively, in the form of longitude-height cross sections taken along the (a) 60°N, (b) 45°N and (c) 25°N latitude circles. Similar cross sections for meridional velocity and temperature fields have also been presented by Saltzman and Sankar Rao (1963). The vertical phase structure of the geo-potential height perturbations is characterized by a distinct westward tilt with height in the middle and higher latitudes (Figs. 2a and 2b). At 25 and 45°N the wave amplitude reaches a peak in the vicinity of the tropopause level (Figs. 2b and 2c), whereas at 60°N it continues to increase with height through the lower stratosphere (Fig. 2a). The abrupt change in the longitudinal phase at about 30°N is evident in the contrast between the patterns in Figs. 2b and 2c.

Maximum amplitudes in the temperature perturbations are located near the earth's surface in the middle and higher latitudes (Figs. 3a and 3b), whereas the strongest perturbations in the subtropics are found at about 300 mb (Fig. 3c). The temperature waves in the middle and higher latitudes are seen to be closely related to the underlying topography, with coldest air lying over the east coasts of the two major continents, and warmest air over the west coasts. Also evident in Fig. 3 is the transition from a vertical structure characteristic of trapped waves at low latitudes, with an out-of-phase relationship between the temperature perturbations in the stratosphere and those in the troposphere, to a structure characteristic of vertically propagating waves at higher latitudes, with a pronounced westward tilt of the temperature perturbations with increasing height.
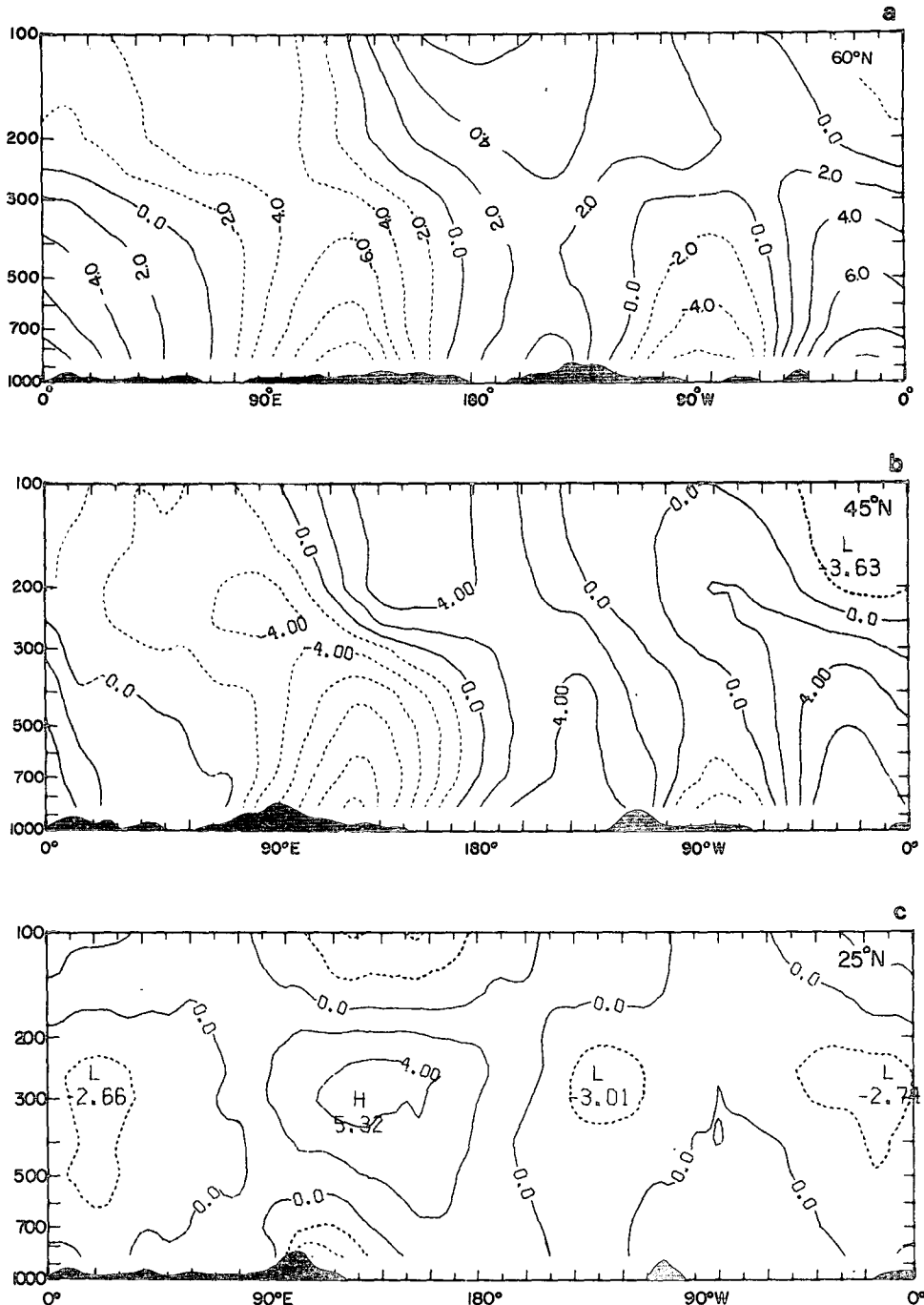

FIG. 3. As in Fig. 2, but for departure from zonal symmetry of the time-averaged temperature field T^*.
Contour interval 2°C.

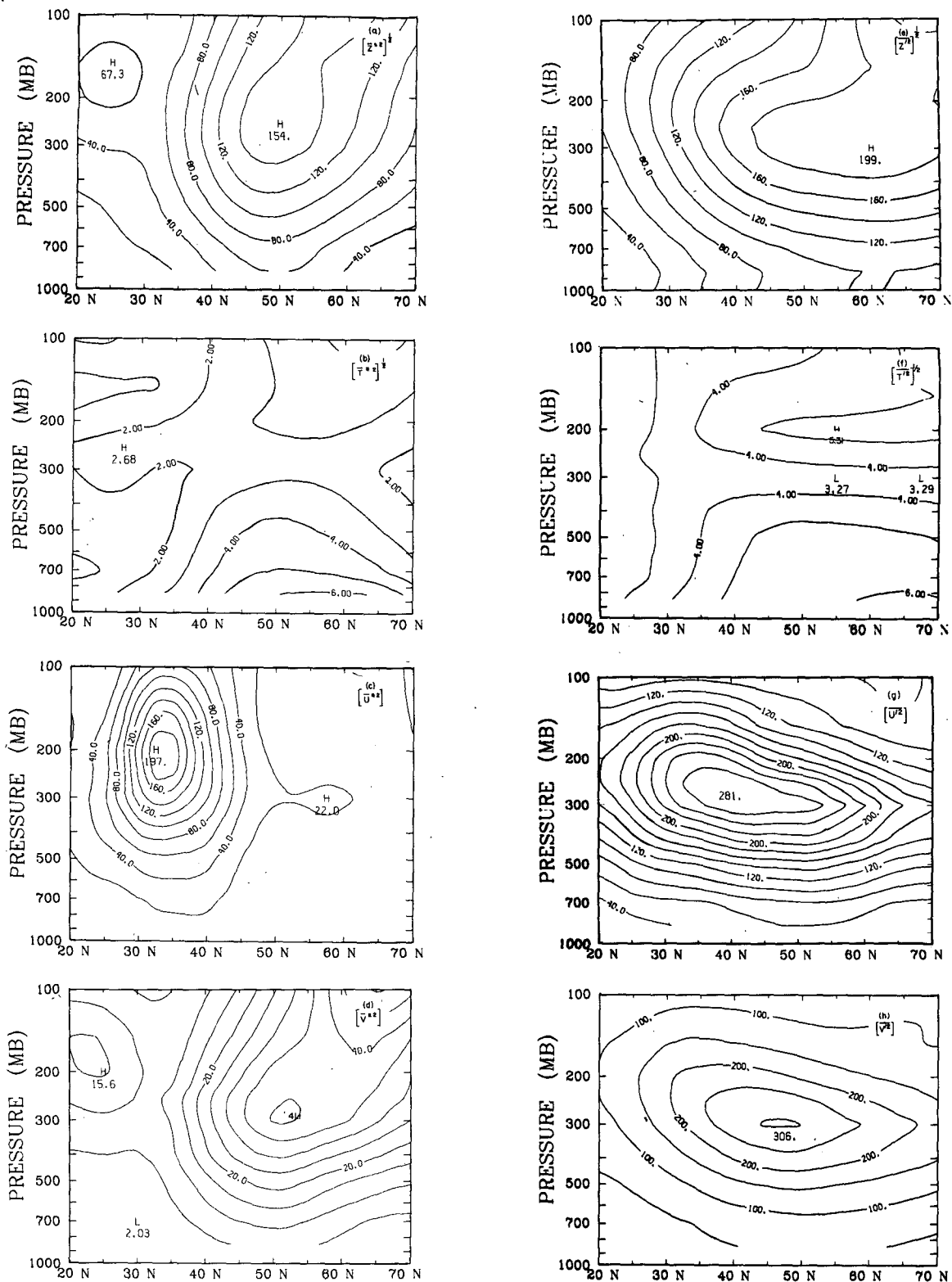FIG. 4. Meridional (latitude-height) cross sections:

(a) $[\bar{z}^{*2}]^{\frac{1}{2}}$, interval 20 m
(b) $[\bar{T}^{*2}]^{\frac{1}{2}}$, interval 1°C
(c) $[\bar{u}^{*2}]$, interval 20 m² s⁻²
(d) $[\bar{v}^{*2}]$, interval 5 m² s⁻²

(e) $[\overline{z'^2}]^{\frac{1}{2}}$, interval 20 m
(f) $[\overline{T'^2}]^{\frac{1}{2}}$, interval 1°C
(g) $[\overline{u'^2}]$, interval 20 m² s⁻²
(h) $[\overline{v'^2}]$, interval 50 m² s⁻².

3. Standing eddy statistics

In this section we shall examine the spatial variances of the time-averaged fields (e.g., $[\bar{u}^{*2}]$, $[\bar{v}^{*2}]$, etc.), and meridional transports by the standing eddies (e.g., $[\overline{v^*T^*}]$, $[\overline{v^*u^*}]$, etc.). Here $[\ ]$ and $\overline{(\ )}$ are the zonal and time averaging operations, respectively, and $(\ )^*$ denotes deviations from the zonally averaged quantity.[3] The distributions of standing eddy statistics presented here can be compared with those compiled by Oort and Rasmusson (1971) using station data, and by Hayashi and Golder (1977) using data from a general circulation model.

a. The standing eddy variance statistics

In Fig. 4 is shown the root-mean-square (rms) statistics of (a) geopotential height $[\bar{z}^{*2}]^{\frac{1}{2}}$ and (b) temperature $[\bar{T}^{*2}]^{\frac{1}{2}}$, as well as the spatial variance of (c) zonal wind $[\bar{u}^{*2}]$ and (d) meridional wind $[\bar{v}^{*2}]$. For comparison, the corresponding distributions for the transient eddies $[\overline{z'^2}]^{\frac{1}{2}}$, $[\overline{T'^2}]^{\frac{1}{2}}$, $[\overline{u'^2}]$ and $[\overline{v'^2}]$, are shown in panels (e) to (h). Here the prime denotes deviations from the time-averaged quantity.[4]

The patterns in Figs. 4a–4d are evidently related to the three-dimensional structure of the stationary perturbations described in Figs. 2 and 3. The standing eddy variance of geopotential height (Fig. 4a) and meridional wind (Fig. 4d) display primary tropospheric maxima near 50°N and 300 mb, and secondary maxima at 25°N and about 200 mb. The spatial variance of temperature (Fig. 4b) display maximum values at about 60°N near the earth's surface, and at 30°N and 300 mb. The maximum in zonal wind variance (Fig. 4c) at 35°N and 200 mb is associated with the strong westerly jets over eastern Asia and eastern North America at this latitude (e.g., see Blackmon et al., 1977, Fig. 6a).

---

[3] The standing eddy statistics presented in this study are obtained by first averaging the atmospheric variables u, v, T, z, etc., over 11 winters, i.e., the overbars appearing in $[\bar{u}^{*2}]$, $[\overline{v^*T^*}]$, etc., represent time averages over 11 winters. It should be noted that these statistics may alternatively be defined by the quantities $[\widetilde{\bar{u}^{*2}}]$, $[\widetilde{v^*T^*}]$, etc., where the tilde represents an average over an individual winter, i.e., the standing eddy statistics are first computed for each winter, and the 11-winter averages of these statistics are then taken. The statistics computed by using the latter method (not shown) generally do not differ from the results presented here by more than 10%.

[4] In the current series of papers, the transient eddy statistics are first computed for each individual winter, and the 11-winter averages of these statistics are then taken, i.e., the primes appearing in $\overline{u'^2}$, $\overline{v'T'}$, etc., represent deviations of the data values within a certain winter from the seasonal average for that particular winter.

b. The meridional transports by standing waves

Fig. 5 shows the meridional transports of (a) heat $[\overline{v^*T^*}]$, (b) westerly momentum $[\overline{v^*u^*}]$ and (c) geopotential energy $[\overline{v^*z^*}]$ by the standing eddies. The corresponding transports by the transient eddies $[\overline{v'T'}]$, $[\overline{v'u'}]$, and $[\overline{v'z'}]$ are shown in Figs. 5d–5f.

The distributions of the stationary eddy transport may also be interpreted in terms of the wave structures depicted in Figs. 1–3. The existence of strong poleward heat transports centered near 50°N (Fig. 5a) is consistent with the westward tilt with altitude of the stationary troughs and ridges at these latitudes, as shown in Figs. 2a and 2b.

The distribution of momentum fluxes in Fig. 5b is characterized by poleward transports south of about 50°N, and equatorward transports north of this latitude. This pattern is related to the southwest-to-northeast tilt of the stationary troughs and ridges over the subtropics, and the southeast-to-northwest tilt in higher latitudes (Fig. 1). The intensity of the standing eddy momentum transports is in agreement with the results of Mak (1978), who noted that his estimates of these statistics based on the Canadian Meteorological Center daily analyses are much larger than those derived from station data by Oort and Rasmusson (1971), probably because of better resolution of the wind field over data sparse regions.

Since the meridional transport of geopotential energy by the geostrophic component of the flow vanishes when averaged around a latitude circle, the distribution of geopotential energy transport in Fig. 5c represents the effects of ageostrophic motions. This pattern is dominated by equatorward transports in the middle latitudes.

When the variance and covariance statistics of the stationary and transient eddies are compared in this zonally averaged context, the contributions by the stationary waves are seen to be relatively weaker. The difference between the magnitudes of $[\bar{v}^{*2}]$ (Fig. 4d) and $[\overline{v'^2}]$ (Fig. 4h) is particularly marked. However, as is demonstrated in Lau (1978, 1979), the effects of these stationary waves play a dominant role in the local, time-averaged balances of momentum and kinetic energy. Hence, the relative importance of the stationary and transient motions cannot be assessed by solely considering these zonally averaged statistics.

4. The time-averaged vorticity balance

a. Diagnosis of the vorticity balance

The relative contributions to the local vorticity budget from the stationary flow and transient motions may be evaluated by examining the following simplified
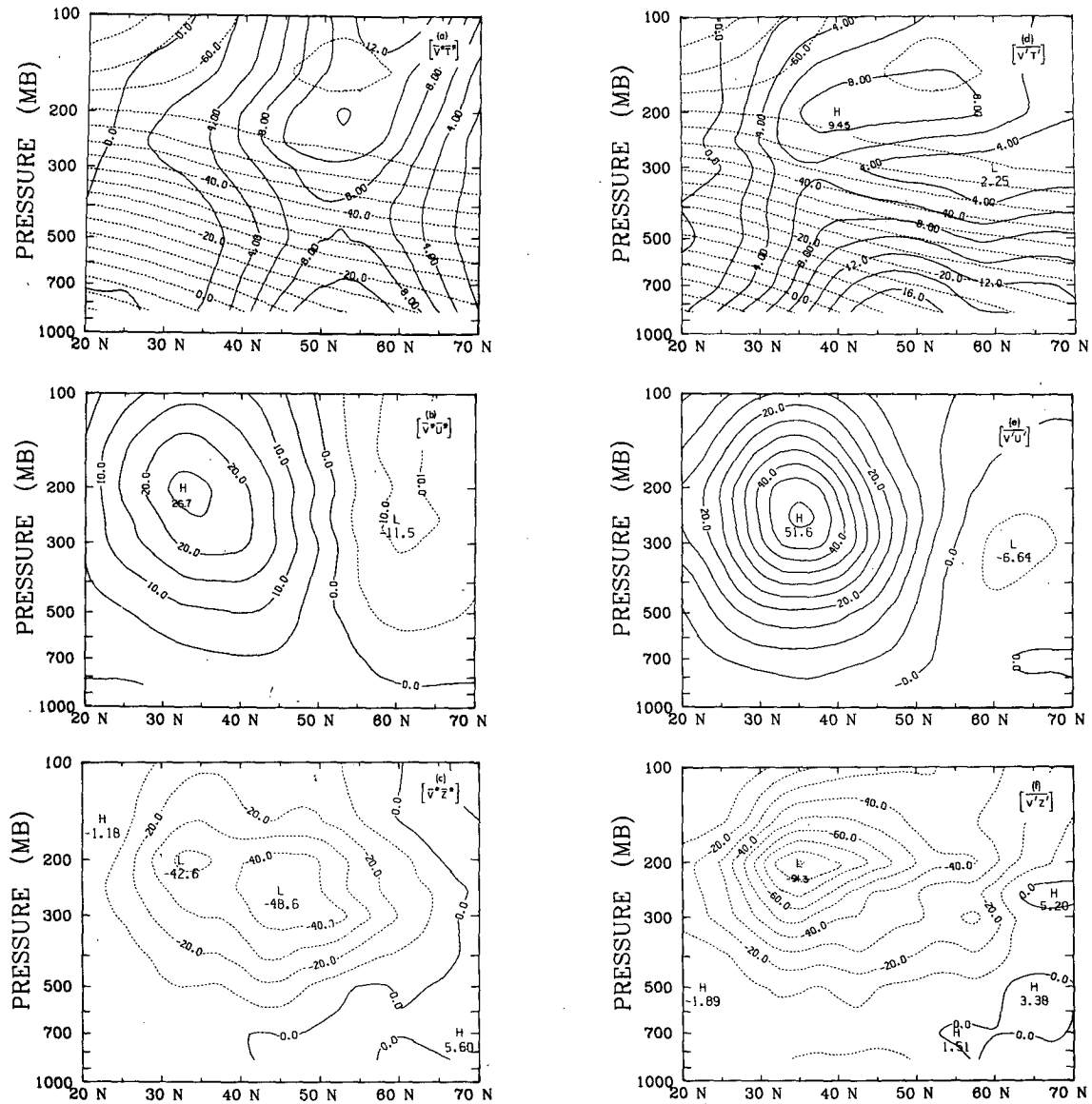
FIG. 5. Meridional (latitude-height) cross sections:

   (a) $[\bar{v}^*\bar{T}^*]$ (solid contours, interval 2°C m s⁻¹) and $[\bar{T}]$ (dashed contours, interval 5°C).

   (b) $[\bar{v}^*\bar{u}^*]$, contour interval 5 m² s⁻²   .

   (c) $[\bar{v}^*\bar{z}^*]$, contour interval 10 m² s⁻¹

   (d) $[\overline{v'T'}]$ (solid contours, interval 2°C m s⁻¹) and $[\bar{T}]$ (dashed contours, interval 5°C)

   (e) $[\overline{v'u'}]$, contour interval 5 m² s⁻²

   (f) $[\overline{v'z'}]$, contour interval 10 m² s⁻¹.

balance equation:

$$\underbrace{-\frac{\bar{u}}{a\cos\phi}\frac{\partial\bar{\zeta}}{\partial\lambda}-\frac{\bar{v}}{a}\frac{\partial}{\partial\phi}(\bar{\zeta}+f)}_{A}$$

$$\underbrace{-\frac{1}{a\cos\phi}\left(\frac{\partial}{\partial\lambda}\overline{u'\zeta'}+\frac{\partial}{\partial\phi}\overline{v'\zeta'}\cos\phi\right)}_{B}$$

$$\underbrace{-(f+\bar{\zeta})\bar{D}_H=0,}_{C}\quad(1)$$

where λ is longitude, ϕ latitude, a earth radius, ζ relative vorticity, f the coriolis parameter and D_H horizontal divergence.

The 300 mb distribution of term A, which represents the local horizontal advection of time-averaged absolute vorticity by the stationary flow, is displayed in Fig. 6a. Since very small-scale irregularities in $\bar{\zeta}$ may lead to
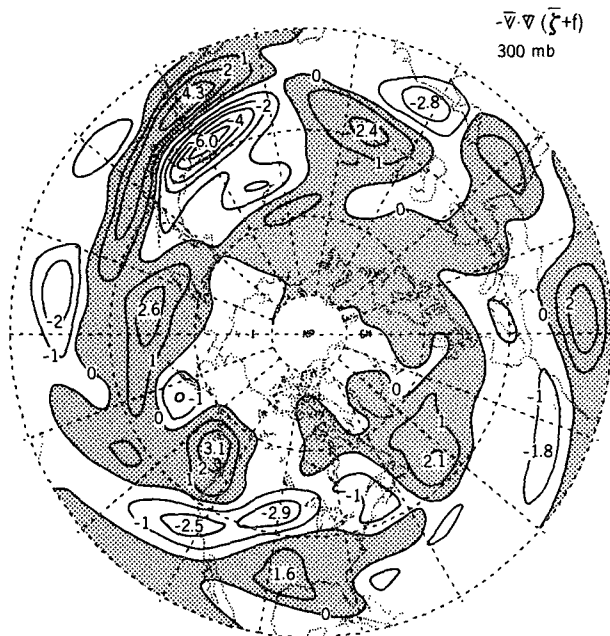
FIG. 6a. Distribution of horizontal advection of absolute vorticity by the time mean flow

$$-\frac{\bar{u}}{a\cos\phi}\frac{\partial\bar{\zeta}}{\partial\lambda}-\frac{\bar{v}}{a}\frac{\partial}{\partial\phi}(\bar{\zeta}+f)$$

at 300 mb. Contour interval 1×10^{-10} s^{-2}.

anomalously large local gradients, the time-averaged vorticity field was smoothed by processing the data through a Fourier filter which retains the first 10 zonal harmonic wavenumbers. It was found that the results were not sensitive to the particular wavenumber cutoff used, as long as the small-scale noise is eliminated.

The hemispheric distributions of the time-averaged streamfunction[5] (solid contours) and absolute vorticity $\bar{\zeta}+f$ (dashed contours) at 300 mb are presented in Fig. 6b. Comparison between Figs. 6a and 6b reveals that the gross features in the former may be accounted for by the rather subtle differences in shape between the streamlines and contours of the absolute vorticity field.

The contributions to term A due to the horizontal advection of (a) relative vorticity $-\bar{V}\cdot\nabla\bar{\zeta}$ and (b) planetary vorticity $-(\bar{v}/a)df/d\phi$ at 300 mb are displayed in Fig. 7. Although these two patterns tend to be negatively correlated with each other, the advection

[5] The streamfunction corresponding to the NMC wind analyses was obtained by solving the Poisson's equation $\nabla^2\bar{\psi}=\bar{\zeta}$, where $\bar{\zeta}$ is the relative vorticity associated with the analyzed wind field. The NCAR software subroutine PWSSSP (NCAR, 1978) was used to invert the Laplacian in spherical coordinates. The boundary condition along the 20°N latitude circle is taken to be $a^{-1}\partial\bar{\psi}/\partial\phi=-\bar{u}(\lambda)$, where $\bar{u}(\lambda)$ is the observed zonal wind at this latitude.

FIG. 6b. Distribution of the time-averaged streamfunction $\bar{\psi}$ (solid contours, interval 10^7 m^2 s^{-1}) and time-averaged absolute vorticity $\bar{\zeta}+f$ (dashed contours, interval 1×10^{-5} s^{-1}) at 300 mb.
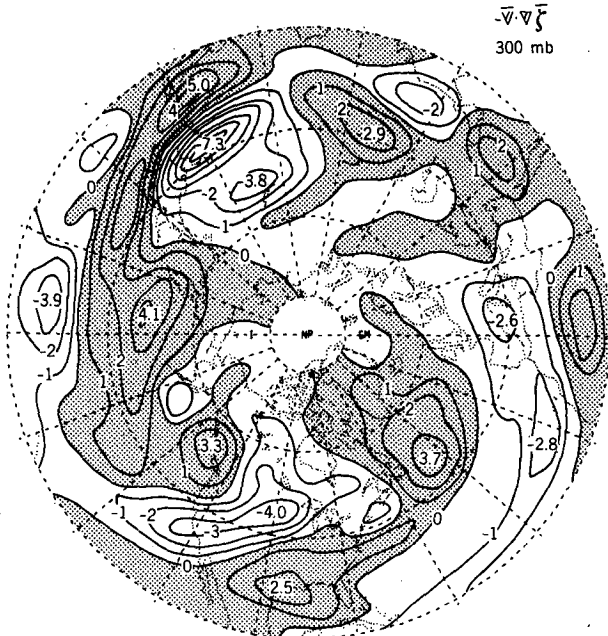
$-\bar{\mathbf{V}}\cdot\nabla\bar{\zeta}$

300 mb

FIG. 7a. Distribution of the horizontal advection of relative vorticity by the time mean flow

$$-\frac{\bar{u}}{a\cos\phi}\frac{\partial\bar{\zeta}}{\partial\lambda}-\frac{\bar{v}}{a}\frac{\partial\bar{\zeta}}{\partial\phi}$$

at 300 mb. Contour interval 1×10^{-10} s^{-2}.

of relative vorticity in the stationary waves (Fig. 7a) is stronger than the β effect (Fig. 7b) by a factor of 3–4; thus the patterns of $-\bar{\mathbf{V}}\cdot\nabla(\bar{\zeta}+f)$ (Fig. 6a) and $-\bar{\mathbf{V}}\cdot\nabla\bar{\zeta}$ (Fig. 7a) bear a strong resemblance to each
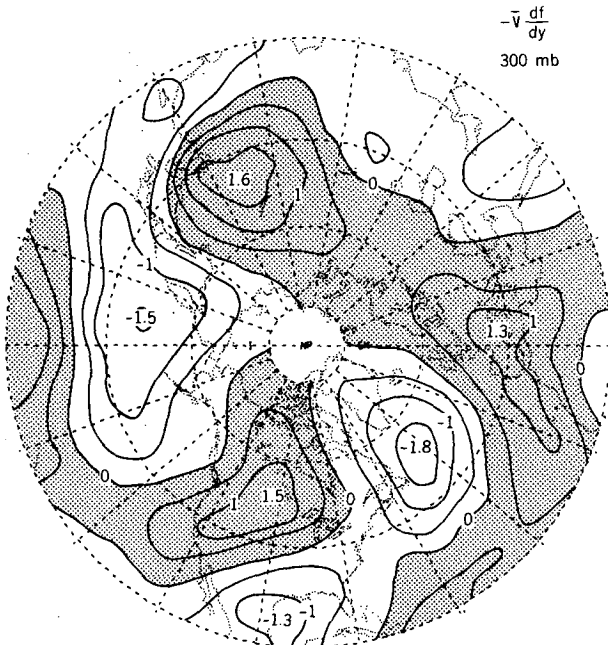
$-\bar{v}\frac{df}{dy}$

300 mb

FIG. 7b. Distribution of the horizontal advection of planetary vorticity by the time mean flow $-(\bar{v}/a)df/d\phi$ at 300 mb. Contour interval 0.5×10^{-10} s^{-2}.

other. This observational result is contrary to the scale analysis applied to ultra-long waves by Burger (1958), who showed that the dominant terms in the vorticity equation on that scale are the divergence term and the β term. Hence it is evident that the forced stationary waves should be regarded as long waves rather than ultra-long waves in scale considerations for the vorticity balance.

In Fig. 8 is shown the 300 mb distribution of the horizontal convergence of vorticity fluxes by transient eddies (term B). The amplitudes of the principal maxima and minima in this figure tend to be weaker than the corresponding values shown in Fig. 6a.

For a steady state situation, the vorticity budget expressed in (1) requires that the composite effects of mean flow advection and eddy flux convergence must be balanced by term C, which is related to the time-averaged divergence $\bar{D}_H$. This mean flow divergence is deduced as a residue of the local vorticity balance at 300 mb, and its distribution is presented in Fig. 9. A strong correlation exists between the major features in this figure and those in Fig. 7a, indicating the dominant role of relative vorticity advection by the mean flow in the vorticity budget.

Results of a diagnosis of the local, time-averaged vorticity balance were recently presented by Holopainen (1978), who made use of circulation statistics derived from station data for the periods 1950-54 and 1958-62. The wintertime distribution of the
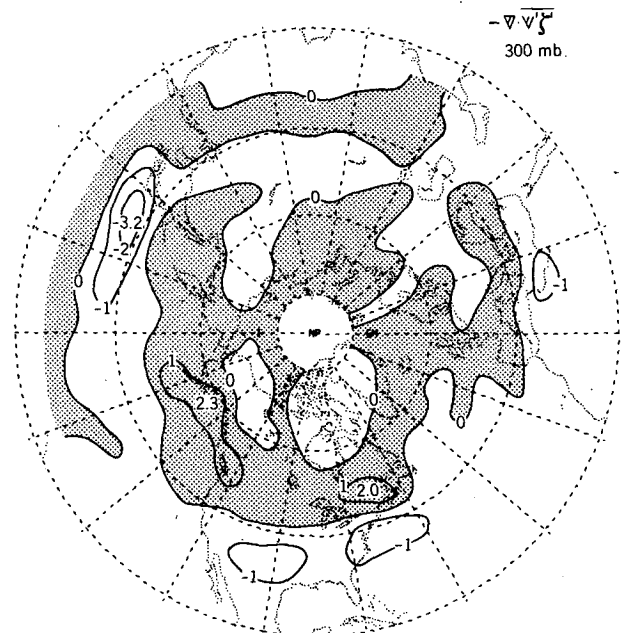
$-\nabla\cdot\overline{\mathbf{V}'\zeta'}$

300 mb

FIG. 8. Distribution of convergence of horizontal vorticity transport by transient eddies

$$-\frac{1}{a\cos\phi}\left(\frac{\partial}{\partial\lambda}\overline{u'\zeta'}+\frac{\partial}{\partial\phi}\overline{v'\zeta'}\cos\phi\right)$$

at 300 mb. Contour interval 1×10^{-10} s^{-2}.

vertically integrated convergence of vorticity fluxes by transient eddies, as shown in Fig. 8 of his paper, is in qualitative agreement with Fig. 8 of the present paper. Holopainen's study indicates that, for annual mean conditions, the vertically integrated values of terms A and B in (1) are comparable in magnitude; whereas our results for the winter season suggest that term A is relatively stronger by a factor of about 2. This may be accounted for by the inclusion of transient fluctuations associated with the seasonal cycle in Holopainen's study, which make substantial contributions to the term B.

Clapp (1956) has also discussed the relative importance of the terms A and B in (1). His estimates of these terms based on limited data records also indicate that the vorticity advection by the stationary flow is stronger than the convergence of eddy vorticity fluxes by a factor of 2–3.

b. Dynamical consistency of $\bar{D}_H$

In order to test the dynamical consistency of the divergence field deduced from vorticity balance considerations, it is useful to consider the following question: Given the divergence forcing function shown in Fig. 9, is it possible to recover the principal features observed in the stationary flow field? As a first approximation, this problem may be addressed by solving for the perturbation streamfunction ψ^* in the linearized vorticity equation

$$\frac{[\bar{u}]}{a\cos\phi}\frac{\partial}{\partial\lambda}\nabla^2\psi^*+\frac{1}{a^2\cos\phi}\frac{\partial\psi^*}{\partial\lambda}\frac{\partial}{\partial\phi}[\bar{\eta}]=-[\bar{\eta}]\bar{D}_H^*$$

$$-\frac{1}{a\cos\phi}\left(\frac{\partial}{\partial\lambda}\overline{u'\zeta'}+\frac{\partial}{\partial\phi}\overline{v'\zeta'}\cos\phi\right)^*,\quad(2)$$

where $[\bar{u}]$ is the zonal mean flow and $[\bar{\eta}]=f-a^{-1}\times(\partial[\bar{u}]/\partial\phi)$ is the absolute vorticity associated with the $[\bar{u}]$ field. By treating $[\bar{u}]$, $\bar{D}_H$ and the convergence of vorticity fluxes by transient motions as known input parameters, Eq. (2) may be solved for ψ^*. The details of this computation are described in the Appendix.

Fig. 10a shows the 300 mb distribution of the perturbation meridional velocity $\bar{v}^*$, which is related to the solution of (2) through the relation

$$\bar{v}^*=\frac{1}{a\cos\phi}\frac{\partial\psi^*}{\partial\lambda}.$$

For comparison, the corresponding distribution obtained by averaging the NMC wind analyses over 11 winters is displayed in Fig. 10b. Except for the fact that the meridional velocities associated with the trough over eastern Asia are stronger by a factor of about 2 in Fig. 10a, there is a strong correspondence between the major features in these two patterns.
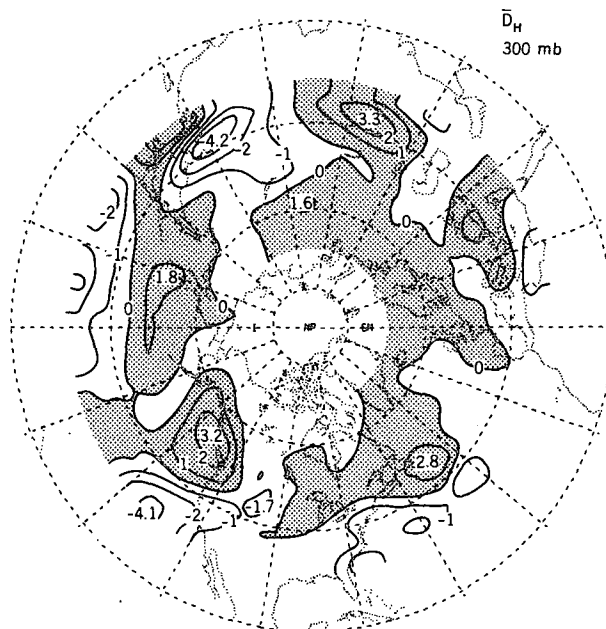

FIG. 9. Distribution of time averaged horizontal divergence $\bar{D}_H$ at 300 mb. Contour interval 1×10^{-6} s^{-1}.

Fig. 11 shows the distribution of the total streamfunction $\bar{\psi}$, as deduced from (a) the solution of the linearized vorticity equation and (b) the NMC wind analyses (refer to footnote 5). Comparison between the two distributions indicates that the essential characteristics of the observed streamfunction are reproduced by the solution of (2).

Fig. 12a presents the contribution to the advection of absolute vorticity by the nonlinear terms

$$\frac{\bar{u}^*}{a\cos\phi}\frac{\partial\bar{\zeta}^*}{\partial\lambda}\frac{\bar{v}^*}{a}\frac{\partial\bar{\zeta}^*}{\partial\phi},$$

the effects of which were not considered in (2). The corresponding contribution by the linear terms

$$\frac{[u]}{a\cos\phi}\frac{\partial\bar{\zeta}^*}{\partial\lambda}\frac{\bar{v}^*}{a}\frac{\partial}{\partial\phi}([\bar{\zeta}]+f)$$

is shown in Fig. 12b. The terms in these figures were computed using the NMC wind analyses at 300 mb. In the vicinity of the stationary trough over eastern Asia, the local values of the linear and nonlinear terms are of the same sign and of comparable magnitude. With the exception of this region, the linear terms are generally stronger than the nonlinear terms. The resemblance between the patterns for the linear terms (Fig. 12b) and for term A (Fig. 6a) further suggests that most of the qualitative features of the vorticity advection term $-\bar{V}\cdot\nabla(\bar{\zeta}+f)$ are retained by the corresponding linearized form. The difference in magnitude between the linear terms and term A
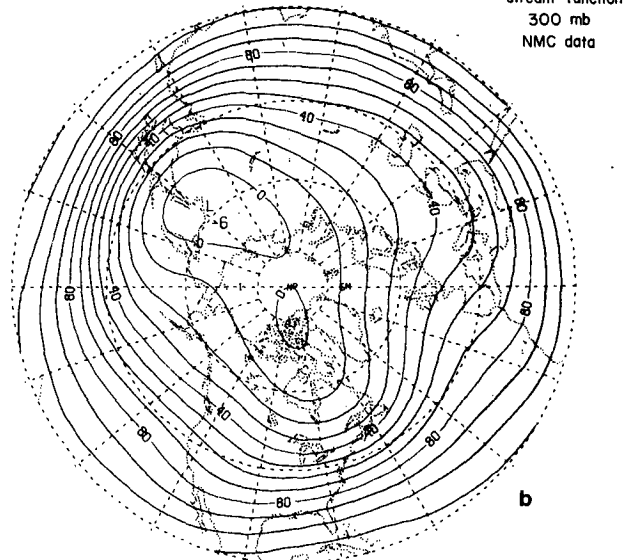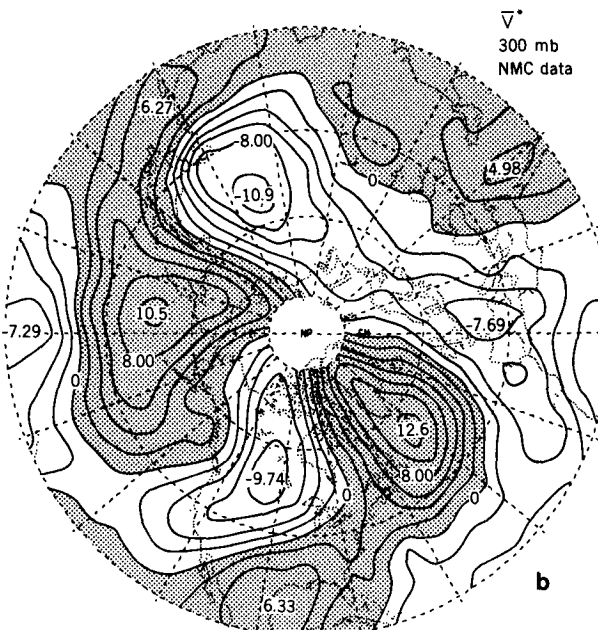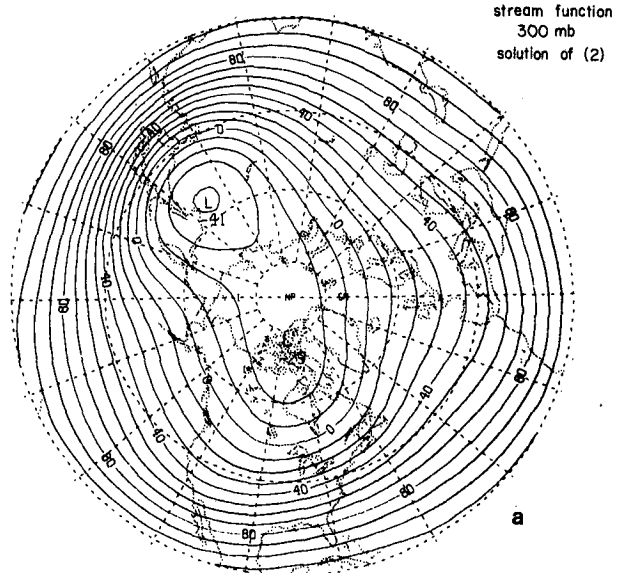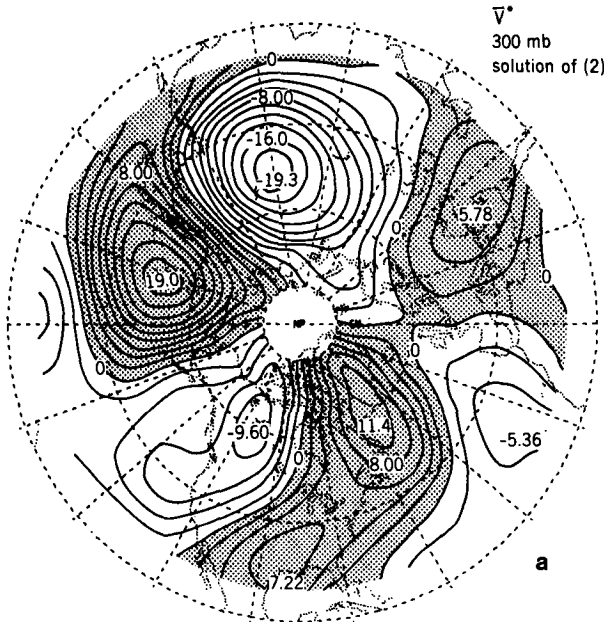
FIG. 10. Distribution of departure from zonal symmetry of the time averaged meridional velocity $\bar{v}^*$ at 300 mb, as obtained for (a) solution of Eq. (2) and (b) NMC data. Contour interval 2 m s⁻¹.

FIG. 11. Distribution of the time-averaged streamfunction $\bar{\psi}$ at 300 mb, as obtained for (a) solution of Eq. (2) and (b) NMC data. Contour interval 10^7 m² s⁻¹.

over northeastern China and northern Pacific is a result of the rather substantial contributions by the nonlinear terms over that region.

Despite the assumption concerning the linearity of the stationary flow field, the results in Figs. 10 and 11 demonstrate the feasibility of retrieving gross features of the stationary wave pattern by using a divergence forcing deduced empirically from vorticity balance considerations. This result indicates that it may be possible to assess the relative importance of orography, diabatic heating and transient motions in maintaining

the stationary flow by solving the linearized vorticity equation (2) with a properly devised divergence function which corresponds to the particular forcing mechanism under consideration.

c. The velocity potential

With a given divergence field, the velocity potential of the mean flow $\bar{\chi}$ may be computed via the relationship[6] $\nabla^2 \bar{\chi} = \bar{D}_H$. The velocity potential corresponding

---

[6] This Poisson's equation is solved by the method described in footnote 5. The boundary condition at the 25°N latitude circle is approximated as $a^{-1}\partial\bar{\chi}/\partial\phi = \bar{v}_a \equiv \bar{v} - \bar{v}_g$, where the subscripts a and g refer to the ageostrophic and geostrophic wind components, respectively.

to the divergence field at 300 mb (Fig. 9) is given in Fig. 13. The divergent component of the stationary flow field $\bar{V}_{DIV}$, as given by $\bar{V}_{DIV} = \nabla \bar{\chi}$, is also depicted as arrows in the same figure. The general pattern of the divergent flow is in good agreement with the longitudinal variation of ageostrophic circulations noted in Lau (1978, Section 6). The divergent flows over the principal jet entry regions (eastern Asia and southwestern United States) are predominantly poleward, whereas equatorward flows prevail in the jet exit regions over the mid-oceans. The typical magnitudes of these divergent flows (2–4 m s^{-1}) are also consistent with the strength of the wind component transverse to the isobars at the jet-stream level, as shown in Blackmon et al., (1977, Fig. 16).

5. The time-averaged vertical velocity field

In the previous section, it was demonstrated that dynamically consistent divergence fields may be deduced through vorticity balance considerations. This suggests that reliable vertical velocity distributions may be obtained by integrating these divergence fields in the vertical direction, i.e.,

$$\bar{\omega}_p - \bar{\omega}_{p_0} = -\int_{p_0}^{p} \bar{D}_H dp, \tag{3}$$

where ω_p denotes the pressure velocity dp/dt at pressure level p, and ω_{p_0} represents the corresponding (assumed

$$-[\bar{u}]\frac{\partial \bar{\zeta}}{\partial x} - \bar{v} \cdot \left(\frac{\partial [\bar{\zeta}]}{\partial y} + f\right)$$
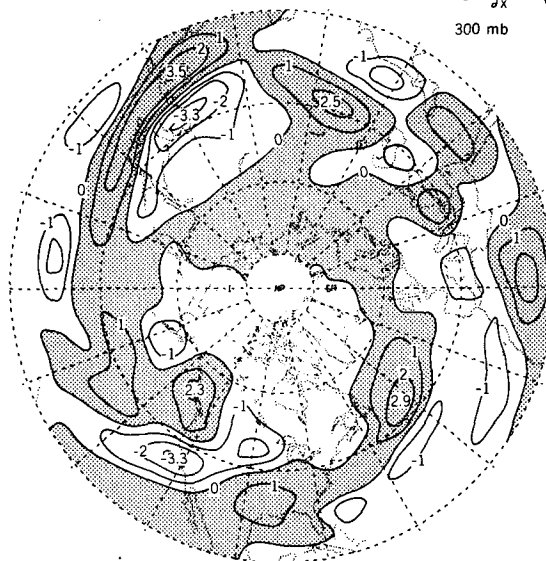300 mb

FIG. 12b. Distribution of the linear terms

$$-\frac{[\bar{u}]}{a\cos\phi}\frac{\partial \bar{\zeta}^*}{\partial \lambda} - \frac{\bar{v}^*}{a}\frac{\partial}{\partial \phi}([\bar{\zeta}]+f)$$

at 300 mb. Contour interval 1×10^{-10} s^{-2}.

known) quantity at level p_0. In order to determine the sensitivity of our results to the choice of boundary conditions, the following computations have been made:

1) The divergence field is integrated downward (in the direction of increasing p) from $p_0 = 100$ mb. $\bar{\omega}_{p_0}$ is assumed to be zero everywhere.
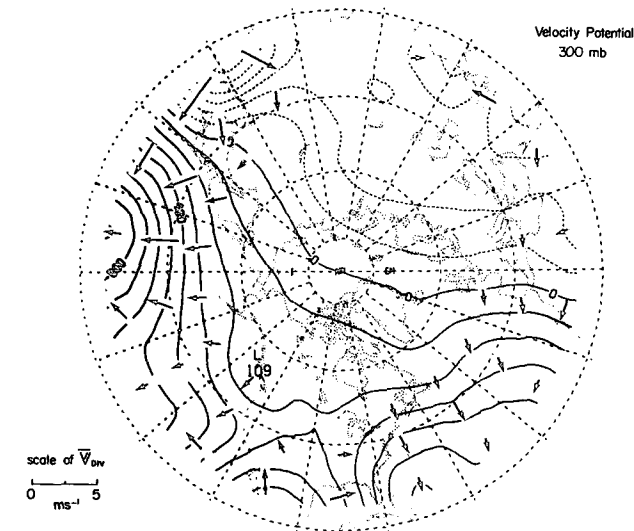
2) The divergence field is integrated upward (in

$$-\bar{V} \cdot \nabla \bar{\zeta}^*$$
300 mb

FIG. 12a. Distribution of the nonlinear terms

$$-\frac{\bar{u}^*}{a\cos\phi}\frac{\partial \bar{\zeta}^*}{\partial \lambda} - \frac{\bar{v}^*}{a}\frac{\partial \bar{\zeta}^*}{\partial \phi}$$

at 300 mb. Contour interval 1×10^{-10} s^{-2}.

Velocity Potential
300 mb

scale of $\bar{V}_{DIV}$

0   5
ms^{-1}

FIG. 13. Distributions of velocity potential (contour interval 1×10^6 m^2 s^{-1}), and divergent flow (arrows) at 300 mb. The length and orientation of the arrows depict the intensity (see scale at lower left) and direction of the local divergent flow, respectively.
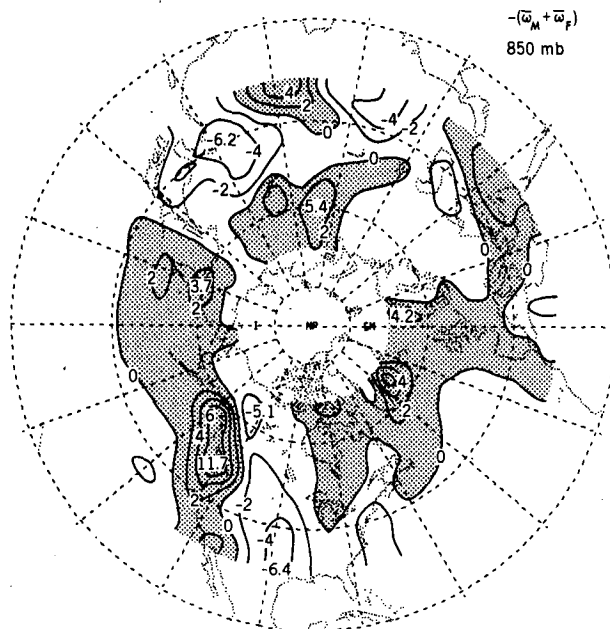
FIG. 14. Distribution of the sum of topographically and frictionally forced pressure velocity $-(\bar{\omega}_M+\bar{\omega}_F)$ at 850 mb. Contour interval 2×10^{-4} mb s^{-1}. Shading indicates rising motion. For conversion from ω to vertical velocity w at 850 mb in middle latitudes, multiply ω in units of 10^{-4} mb s^{-1} by 0.1 to obtain w in units of cm s^{-1}.

the direction of decreasing p) from $p_0 = 850$ mb; the pressure velocity at the lower boundary is assumed to be

$$\bar{\omega}_{p_0} = \bar{\omega}_M + \bar{\omega}_F,$$

where

$$\bar{\omega}_M = -\frac{1}{\rho g}\bar{\mathbf{v}}\cdot\nabla h,$$

$$\bar{\omega}_F = -\frac{\sin2\beta}{\rho g}\left(\frac{K}{2f}\right)^{\frac{1}{2}}\bar{\zeta}_g$$

are the orographically and frictionally forced vertical motions, respectively. Here ρ is the air density, g gravity, h the height of the local terrain [as tabulated by Berkofsky and Bertoni (1955)], β the angle between the isobars and the local wind vector, assumed to be 22.5°, K the eddy diffusivity, assumed to be 10 m^2 s^{-1} [the values used by Charney and Eliassen (1949)] and $\bar{\zeta}_g$ the geostrophic relative vorticity. The distribution of $-(\bar{\omega}_M+\bar{\omega}_F)$, as computed using data at 850 mb, is shown in Fig. 14.

This result may be compared with the distribution of $\bar{\omega}_M$ computed by Saltzman and Irsch[7] (1972, Fig. 1) using observed wind data at 850 and 700 mb, and the

smoothed topographic heights of Berkofsky and Bertoni (1955); and that of $\bar{\omega}$ analyzed by Hayashi and Golder (1977, Fig. 5.4) using data from a general circulation experiment.

3) The divergence $\bar{D}_H$ in the integrand of (3) is adjusted so that the boundary conditions at 100 mb ($\bar{\omega}_{100\text{ mb}} = 0$) and 850 mb ($\bar{\omega}_{850\text{ mb}} = \bar{\omega}_M + \bar{\omega}_F$) are both satisfied. Following the suggestion of O'Brien (1970), the divergence adjustment is assumed to be a linear function of pressure, i.e.

$$\bar{\omega}_p - \bar{\omega}_{p_B} = -\int_{p_B}^{p}\bar{D}_H dp + (\bar{\omega}_{p_T}-\bar{\omega}_T)\frac{(p-p_B)^2}{(p_T-p_B)^2},$$

where $p_B = 850$ mb, $p_T = 100$ mb, $\bar{\omega}_{p_B} = \bar{\omega}_M + \bar{\omega}_F$, $\bar{\omega}_{p_T} = 0$, and

$$\bar{\omega}_T = -\int_{p_B}^{p_T}\bar{D}_H dp + \bar{\omega}_{p_B}.$$

The distributions of the time-averaged pressure velocity at 500 mb, as evaluated by the above methods, are presented in Figs. 15a–15c. Despite the different boundary conditions used in Figs. 15a and 15b, there is a considerable degree of resemblance between the two patterns. Moreover, the two methods yield maxima and minima of similar magnitudes. The distributions in Fig. 15 are in qualitative agreement with mean vertical motion fields generated by the NMC numerical weather prediction models (Lau, 1979, Fig. 1) and by a general circulation model (Manabe and Holloway, 1975, Fig. 5). The principal features in Fig. 15 are also consistent with the hemispheric distributions of mean precipitation, as estimated by Möller (1951) and reproduced by Manabe and Holloway (1975, Fig. 13), and mean cloud coverage, as deduced from satellite measurements (U.S. Dept. of Commerce and U.S. Air Force, 1971, p. 106).

The maritime features in Fig. 15 are characterized by ascent of air over most of the oceanic areas in the middle and higher latitudes, and large-scale subsidence over the eastern oceans in the subtropics. The distributions over continental regions are closely related to the underlying topography, with strong rising motions to the west of the major mountain ranges and strong sinking motions to the east. These characteristics also support the postulated existence of time-averaged, thermally direct meridional circulations over the jet entry regions, and thermally indirect circulations over the jet exit regions [e.g., see the discussion in Blackmon et al. (1977, Section 8d)]. It is noted that the above features are not solely confined to the distributions in Figs. 15b and 15c, which are dependent on the assumed vertical motion field at 850 mb; they are just as evident in Fig. 15a, which is obtained without imposing any constraint at the lower boundary.

[7] Prof. B. Saltzman (private communication) has noted that the values of $\bar{\omega}_M$ presented in Figs. 1, 2 and 3 of Saltzman and Irsch are actually expressed in units of 10^{-1} cm s^{-1} instead of 10^{-2} cm s^{-1}.

6. Standing eddy statistics derived from mean vertical motion fields

We now make use of the vertical velocity fields derived by the method described in Section 5c to compute the standing eddy statistics involving vertical motions. Similar statistics have previously been compiled by Molla and Loisel (1962) and Oort and Rasmusson (1971) from station data as well as by Hayashi and Golder (1977) for the output from a general circulation model.

The zonally averaged distribution of mean vertical velocity, $-[\bar{\omega}]$, shown in Fig. 16a, is characterized by sinking motions equatorward of about 45°N and rising
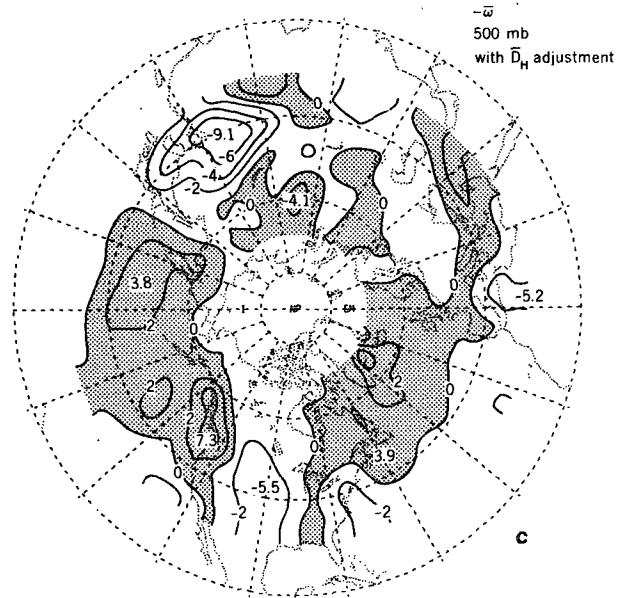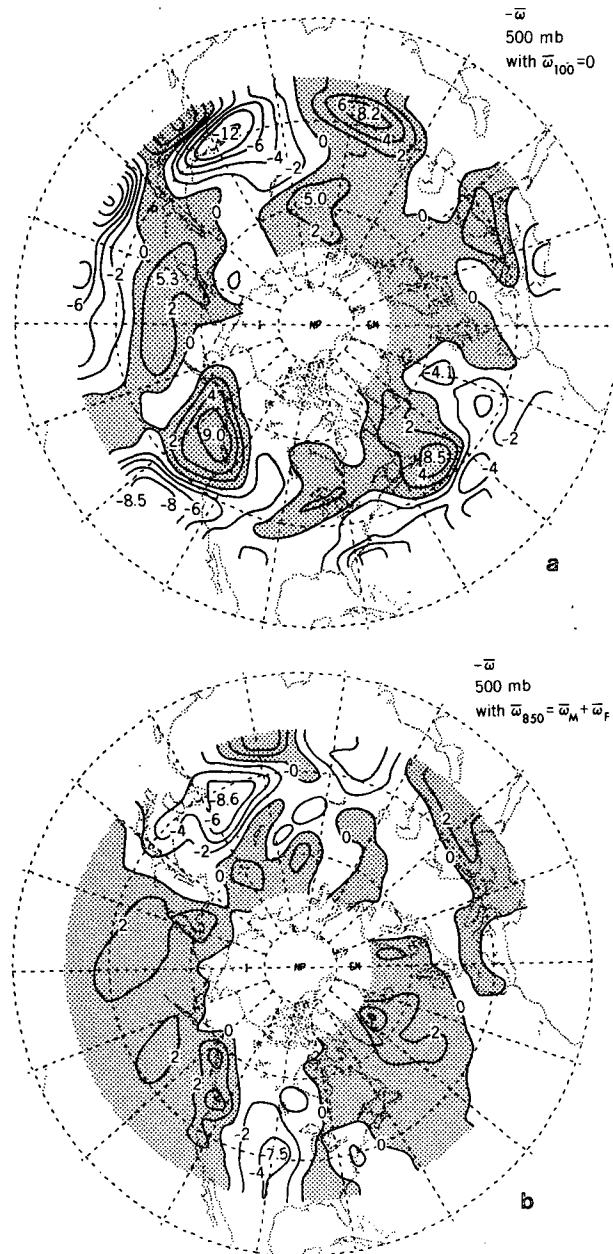
FIG. 15. Distributions of pressure velocity $-\bar{\omega}$ at 500 mb, as obtained by (a) integrating $\hat{D}_H$ downward from the 100 mb level, (b) integrating $\hat{D}_H$ upward from the 850 mb level, and (c) matching boundary conditions at the 100 and 850 mb levels. Contour interval 2×10^{-4} mb s^{-1}. Shading indicates rising motion. For conversion from ω to vertical velocity w at 500 mb in midlatitudes, multiply ω in units of 10^{-4} mb s^{-1} by 0.15 to obtain w in units of cm s^{-1}.

motion north of that latitude. The intensity of the upward and downward branches of this Ferrel circulation reaches up to about 10^{-4} mb s^{-1} (or 0.1 cm s^{-1}). The spatial variance of the vertical velocity field $[\bar{\omega}^{*2}]$ is shown in Fig. 16b.

Fig. 16c shows the covariance in space between vertical motion and temperature, $-[\bar{\omega}^*\bar{T}^*]$. The stationary motions over regions poleward of about 35°N are generally characterized by ascent of warm air and descent of cold air $(-[\bar{\omega}^*\bar{T}^*]>0)$. On the other hand, the stationary fields of temperature and vertical motion are seen to be negatively correlated over the subtropics. The covariance between vertical and meridional motions, $-[\bar{\omega}^*\bar{v}^*]$, is presented in Fig. 16d. Except for the region in the vicinity of the zonal mean jet, the upward and poleward motions in the stationary waves are positively correlated.

In Fig. 17a the meridional and vertical fluxes of geopotential energy $([\bar{v}^*\bar{z}^*], [\bar{w}^*\bar{z}^*])$ are represented using a vectorial format. The vertical and meridional flux components are scaled in the same ratio as that between the height and latitude axes of the meridional cross section. Superimposed on this flux vector pattern is the distribution of kinetic energy in the stationary waves, $\frac{1}{2}[\bar{u}^{*2}+\bar{v}^{*2}]$. The middle and upper troposphere is characterized by upward and equatorward transports of geopotential energy north of about 35°N. On the other hand, downward transports prevail in the subtropics. There is a noticeable convergence of
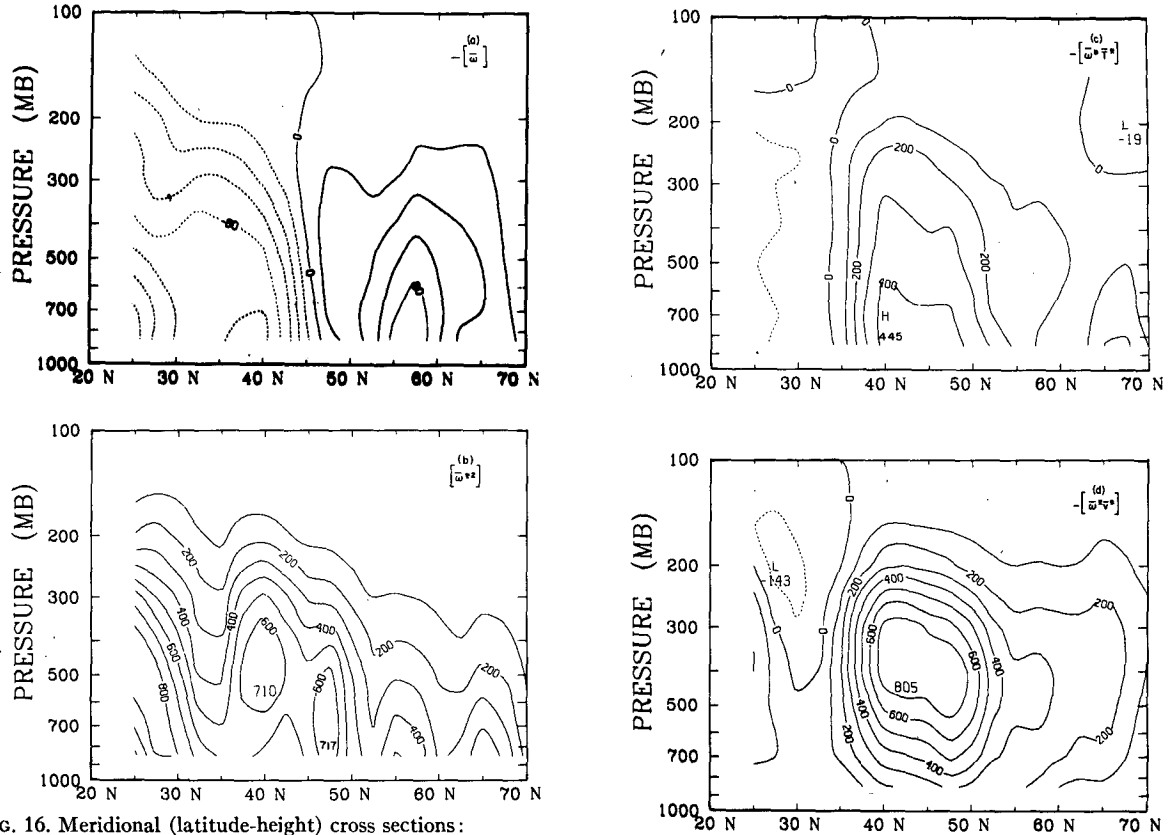
FIG. 16. Meridional (latitude-height) cross sections:

(a) $-[\bar{\omega}]$, interval 2×10^{-5} mb s^{-1}
(b) $[\bar{\omega}^{*2}]$, interval 1×10^{-8} mb^2 s^{-2}

(c) $-[\bar{\omega}^*\bar{T}^*]$, interval 1×10^{-4} °C mb s^{-1}
(d) $-[\bar{\omega}^*\bar{v}^*]$, interval 1×10^{-4} m mb s^{-2}.

geopotential energy transports in the vicinity of the subtropical jet. The general pattern suggests that the enhanced kinetic energy associated with the wintertime jet streams in the 30–40°N latitude belt is maintained by geopotential energy transports which originate from higher latitudes. This result is consistent with the analysis of stationary waves appearing in a general circulation model developed at the Geophysical Fluid Dynamics Laboratory, as presented by Hayashi and Golder (1977, Fig. 5.8).

The meridional and vertical transports of westerly momentum by the stationary waves ($[\bar{v}^*\bar{u}^*]$, $[\bar{\omega}^*\bar{u}^*]$) are displayed in Fig. 17b, together with the distribution of $[\bar{u}]/\cos\phi$. This pattern is dominated by the meridional component of the momentum transport (see Fig. 5b). The region between 35 and 50°N is characterized by down-gradient transport of momentum, whereas the transports are mostly up-gradient over the subtropics.

7. The heat balance and the distribution of diabatic heating

The geographical distribution of diabatic heating in the atmosphere has been a subject of interest in several earlier investigations. Smagorinsky (1953) and Clapp (1961) have deduced the atmospheric heating

rate by considering a variety of physical processes such as condensation, radiation and sensible heat transfer. Clapp (1961), Brown (1964) and Geller and Avery (1978) determined the local diabatic heating as a residue of the thermodynamic energy equation. One of the difficulties with the latter approach is the uncertainties inherent in the circulation statistics involving vertical motions. In the present study, vertical velocity fields deduced from the vorticity budget (Section 5c) are used to evaluate the vertical advection terms in the thermodynamic energy equation.

The time-averaged thermodynamic energy equation may be written as

$$\underbrace{\frac{\bar{u}}{a\cos\phi}\frac{\partial\bar{T}}{\partial\lambda}-\frac{\bar{v}}{a}\frac{\partial\bar{T}}{\partial\phi}}_{A}\underbrace{-\bar{\omega}\left(\frac{\partial\bar{T}}{\partial p}-\frac{R\bar{T}}{pC_p}\right)}_{B}$$

$$\underbrace{-\frac{1}{a\cos\phi}\left(\frac{\partial}{\partial\lambda}\overline{u'T'}+\frac{\partial}{\partial\phi}\overline{v'T'}\cos\phi\right)}_{C}$$

$$\underbrace{-\frac{\partial}{\partial p}\overline{\omega'T'}+\frac{R}{pC_p}\overline{\omega'T'}}_{D}+\bar{Q}=0, \quad (4)$$

where R is the gas constant, C_p the specific heat at constant pressure, and Q the diabatic heating rate in units of °C per unit time. The term A represents temperature advection by the horizontal component of the stationary flow; term B represents the effects of time mean vertical motions in advecting heat and in producing temperature changes due to adiabatic expansion and compression; and term C represents the convergence of horizontal heat transports by the transient eddies. The effects of vertical eddy transports by transient eddies, $\overline{\omega'T'}$, on the heat balance are given by term D. The statistics on $\overline{\omega'T'}$ at 700 mb have been compiled by Lau (1979, Fig. 4) using twice-daily NMC forecast fields of vertical motion. With the assumption that $\overline{\omega'T'}=0$ at sea level and at the tropopause, it can be shown that the largest absolute values of the terms $\partial\overline{\omega'T'}/\partial p$ and $(R/pC_p)\overline{\omega'T'}$, which occur over the principal oceanic storm tracks, are respectively less than 1°C day^{-1} and 0.2°C day^{-1} at most levels in the troposphere. As will be demonstrated presently, since the net heating rates over the oceanic storm tracks are typically more than 2°C day^{-1}, it is justifiable to neglect the term D in the following consideration of the heat balance.
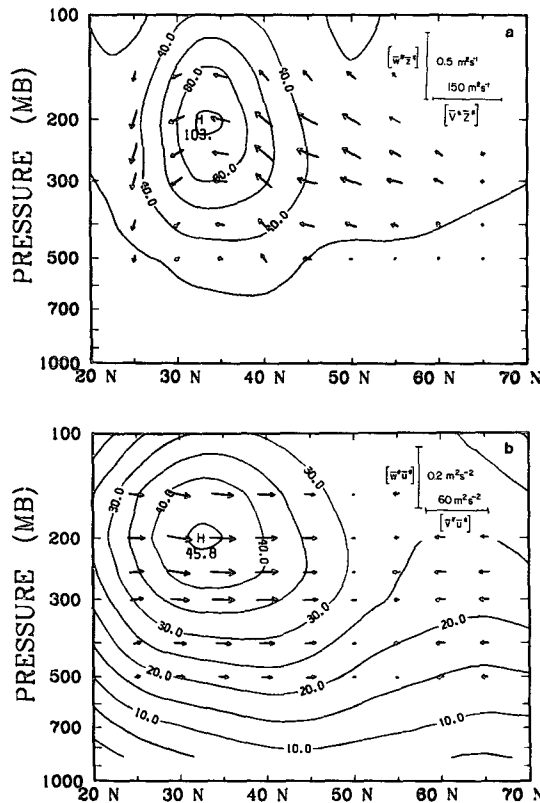

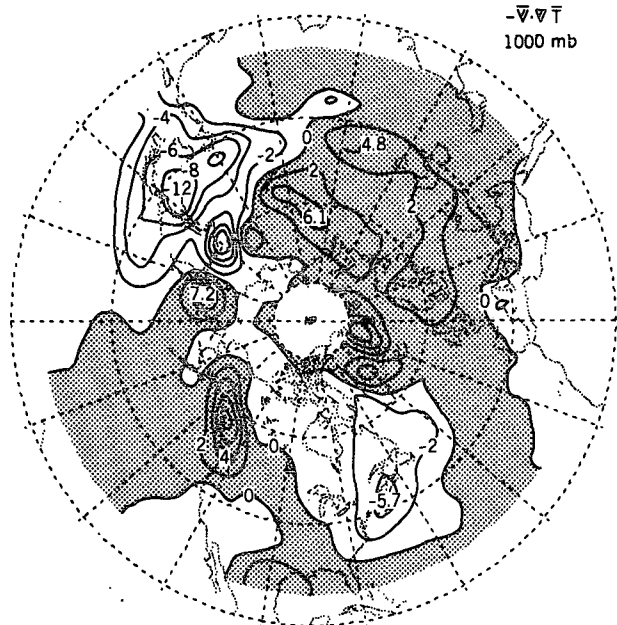FIG. 18a. Distribution of horizontal advection of heat by the time mean flow

$$-\frac{\bar{u}}{a\cos\phi}\frac{\partial\bar{T}}{\partial\lambda}-\frac{\bar{v}}{a}\frac{\partial\bar{T}}{\partial\phi}$$
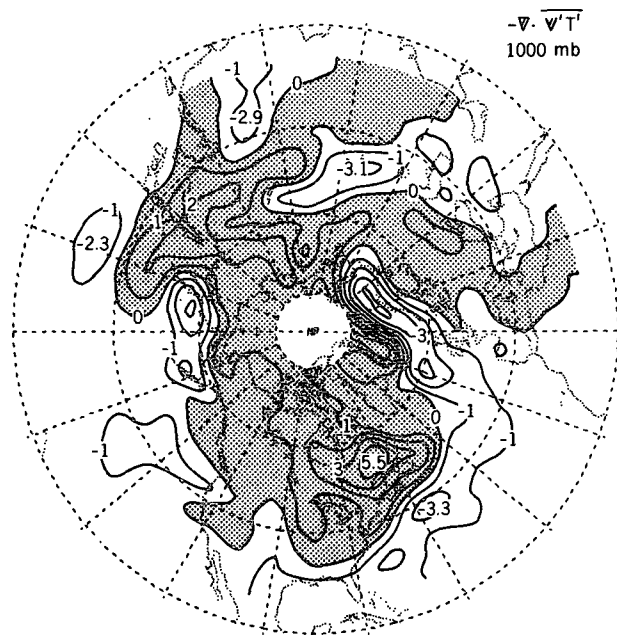
at 1000 mb. Contour interval 2°C day^{-1}.

FIG. 18b. Distribution of convergence of horizontal heat transport by transient eddies

$$-\frac{1}{a\cos\phi}\left(\frac{\partial}{\partial\lambda}\overline{u'T'}+\frac{\partial}{\partial\phi}\overline{v'T'}\cos\phi\right)$$

at 1000 mb. Contour interval 1°C day^{-1}.

FIG. 17. Meridional (latitude-height) cross sections of (a) $\frac{1}{2}[\bar{u}^{*2}+\bar{v}^{*2}]$ (contour interval 20 m² s^{-2}) and vector fluxes of geopotential energy by standing waves ($[\bar{v}^*\bar{z}^*]$, $[\bar{w}^*\bar{z}^*]$), and (b) $[\bar{u}]/\cos\phi$ (contour interval 5 m s^{-1}) and vector fluxes of westerly momentum by standing waves ($[\bar{v}^*\bar{u}^*]$, $[\bar{w}^*\bar{u}^*]$).
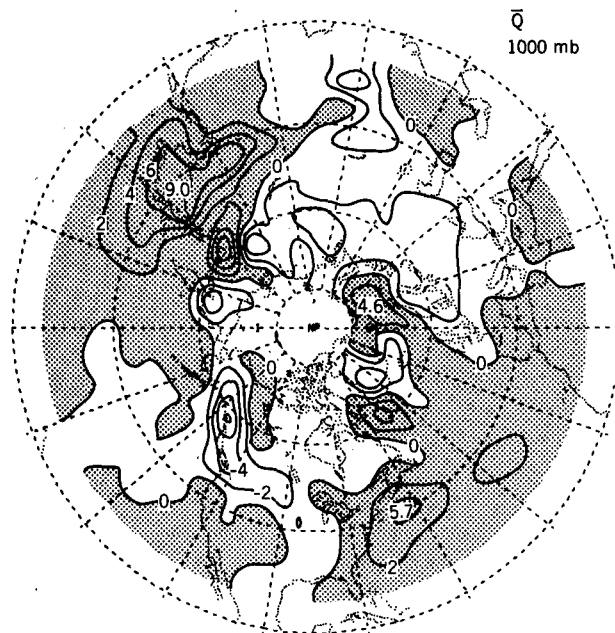
FIG. 19. Distribution of diabatic heating rate $\bar{Q}$ at 1000 mb.
Contour interval 2°C day^{-1}.

a. 1000 mb level

Over the oceans as well as continental regions with low terrain, the mean vertical velocity at the 1000 mb level may be assumed to be zero, and the local heat balance is primarily determined by the stationary and transient components of the horizontal transports. The distributions of the terms A and C at 1000 mb are shown in Fig. 18a and 18b, respectively.[8] The eastern portions of the Asian and North American continents, and the adjacent oceanic areas, are under the influence of cold advection by the northerly circulation west of the Aleutian and Icelandic low pressure centers (Fig. 18a). On the other hand, the predominantly southerly flow over the western continents accounts for the warm advection observed over those regions. The convergence of the transient eddy heat transports (Fig. 18b) is generally characterized by flux divergence south of the centers of baroclinic activity over the western oceans (see Blackmon et al., 1977, Figs. 1 and 2); and flux convergence to the north of these regions. Strong divergences are also observed over the waters of the Bering Sea and the Arctic Ocean north of Europe, which are remarkably warm for their respective latitudes. Over the Pacific and eastern Asia, the contributions of eddy heat fluxes to the local heat budget are weaker than those of the mean flow advection by a factor of 2–3. Throughout much of the remainder of the Northern Hemisphere, terms A and C in (4) are of comparable magnitude.

---

[8] The circulation statistics at 1000 mb were compiled by using geostrophic winds. The results at all other levels were deduced from the NMC analyzed wind data.

The distribution of the diabatic heating rate at 1000 mb, as computed by neglecting the terms B and D, is given in Fig. 19.[9] The maxima in diabatic heating over the western oceans are associated with the upward transfer of sensible heat from the warm Kuroshio and Gulf Stream currents underlying these regions (e.g., see Bunker, 1976), whereas the prevalent cooling over continental regions is essentially a result of sensible heat loss (Clapp, 1961). The strong cooling along the coasts of Alaska and British Columbia should be viewed with caution, since neither the use of the geostrophic temperature advection nor the neglect of the effects of vertical motions are justified in this region of strong terrain influences.

b. 700 mb level

The distributions of the terms A and B in (4) at 700 mb are shown in Figs. 20a and 20b, respectively. The horizontal temperature advection by the mean flow at 700 mb (Fig. 20a) is dominated by cold advection over the eastern portion of the major continents and by warm advection over the west coast of North America and over western Siberia.

The pattern of the adiabatic temperature change induced by mean vertical motion (Fig. 20b) bears distinct signatures of topographical effects, with cooling on the windward side of the major mountain ranges and warming over the leeward side. There is a tendency for cancellation between terms A and B; however, with the exception of regions of high terrain, the horizontal temperature advection term is larger by a factor of about 2.

The distribution of term C in (4) at 700 mb, shown in Fig. 20c, is similar to that at 1000 mb (Fig. 18b) except for the strong flux divergence over the west coast of North America, which is a result of strong eastward eddy fluxes of heat $(\overline{u'T'})$ over and just to the lee of the Rockies. A parallel feature is also evident along the west coast of northern Europe. The enhanced correlation between zonal winds and temperature over these regions may be a consequence of the intermittent eastward intrusions of warm maritime air $(T'>0)$ in a strong westerly flow regime $(u'>0)$.

Taking into account the processes represented by terms A, B and C in (4), the horizontal distribution of the diabatic heating rate at 700 mb may be deduced as a residue. The result is shown in Fig. 21. The locations of most of the principal maxima and minima are similar to those in the corresponding distribution at

---

[9] Since geostrophic winds were used for the 1000 mb level, the heating rates given in Fig. 19 may be overestimated. The diabatic heating field in this figure may alternatively be interpreted as pertaining to the top of the planetary boundary layer, where the geostrophic horizontal temperature advections are more representative of the true advections and the neglect of term B in (4) is still a good approximation.

1000 mb (Fig. 19), although the magnitudes are reduced by a factor of about 2.

It is interesting to note that there is a strong correspondence between the patterns of eddy heat flux convergence at 700 mb (Fig. 20c) and the zonally asymmetric component of the time-averaged 700 mb temperature field ($\bar{T}^*$), which is virtually identical in shape to the 850–300 mb thickness pattern shown in Fig. 1. The heat transports by transient eddies are strongly convergent over northeastern Asia and northeastern Canada, where they act to dissipate the negative anomalies in the stationary temperature field. Similarly, the predominantly divergent heat transports over the eastern oceans tend to destroy the positive temperature anomalies at those locations. This relationship may be described in more quantitative terms by decomposing the 700 mb distributions of horizontal heat flux divergence ($\nabla \cdot \overline{v'T'}$) and mean temperature ($\bar{T}$) into zonal harmonic components along selected latitude circles. The amplitude and phase corresponding to the first four zonal wavenumbers of these fields are presented in Table 1. The time scales associated with the dissipative effects of the transient eddies are given in the last column of the table. These estimates are obtained by taking the ratio of the amplitudes of mean temperature and heat flux divergence corresponding to the same latitude and zonal wavenumber. The data in Table 1 confirm that the phases of the two fields in middle and high latitudes exhibit a strong
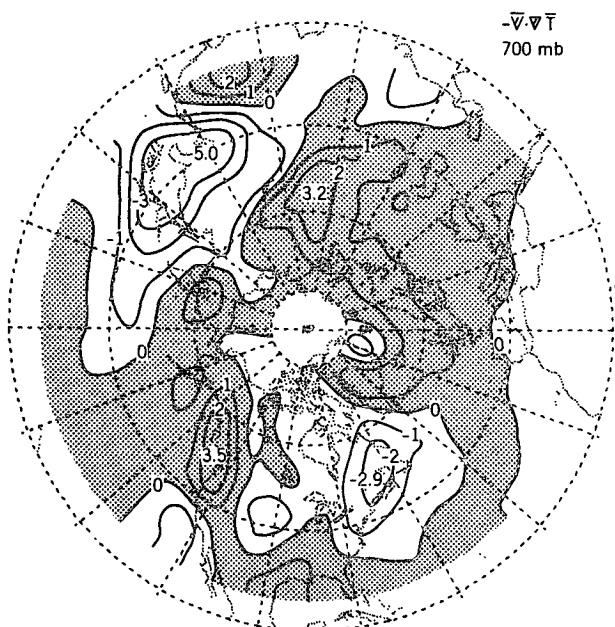
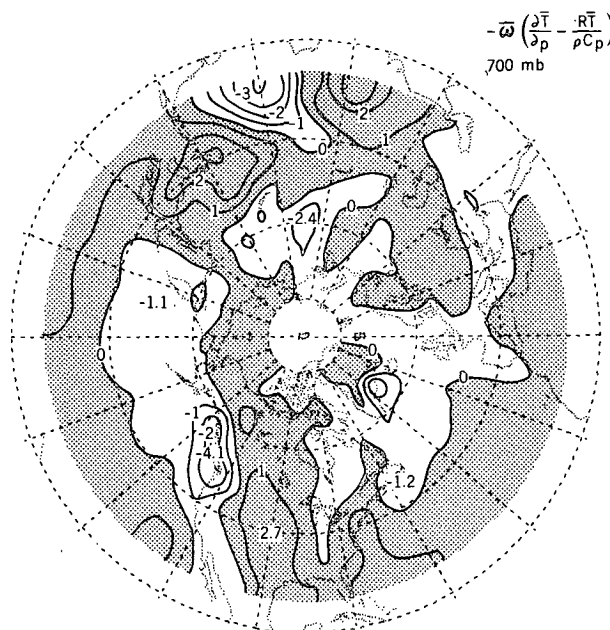$$-\bar{\omega}\left(\frac{\partial \bar{T}}{\partial p} - \frac{R\bar{T}}{pC_p}\right)$$
700 mb

FIG. 20b. Distribution of adiabatic heating term

$$-\bar{\omega}\left(\frac{\partial \bar{T}}{\partial p} - \frac{R\bar{T}}{pC_p}\right)$$

at 700 mb. Contour interval 1°C day^{-1}.
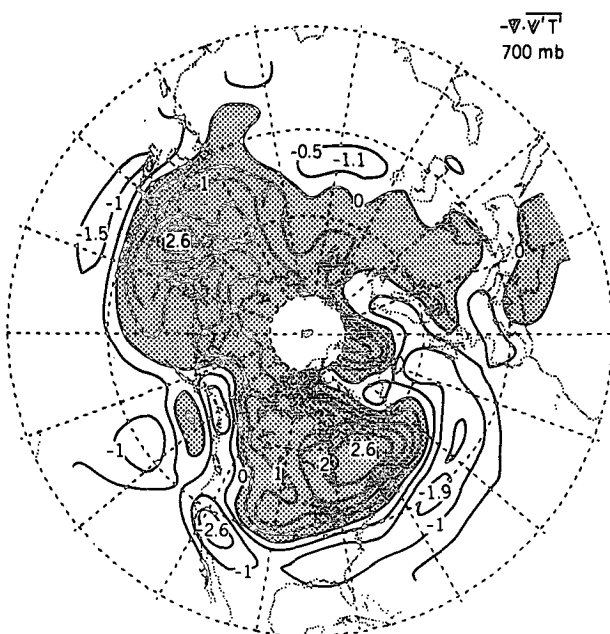
$$-\overline{\nabla} \cdot \nabla \bar{T}$$
700 mb

FIG. 20a. Distribution of horizontal advection of heat by the time mean flow

$$-\frac{\bar{u}}{a\cos\phi}\frac{\partial \bar{T}}{\partial \lambda} - \frac{\bar{v}}{a}\frac{\partial \bar{T}}{\partial \phi}$$

at 700 mb. Contour interval 1°C day^{-1}.

$$-\nabla \cdot \overline{v'T'}$$
700 mb

FIG. 20c. Distribution of convergence of horizontal heat transport by transient eddies

$$-\frac{1}{a\cos\phi}\left(\frac{\partial}{\partial \lambda}\overline{u'T'} + \frac{\partial}{\partial \phi}\overline{v'T'}\cos\phi\right)$$

at 700 mb. Contour interval 0.5°C day^{-1}.

TABLE 1. The amplitude and phase corresponding to the first four zonal wavenumbers of the 700 mb distributions of $\nabla \cdot \overline{v'T'}$ and $\bar{T}$ at selected latitude circles. The time scales (τ) in the last column are obtained by taking the ratio of the amplitudes of $\bar{T}$ and $\nabla \cdot \overline{v'T'}$ corresponding to a given latitude and a given wavenumber.

Latitude	Zonal wavenumber	Phase $\bar{T}$	Phase $\nabla \cdot \overline{v'T'}$	Amplitude $\bar{T}$ (°C)	Amplitude $\nabla \cdot \overline{v'T'}$ (°C day^{-1})	τ (days)
40°N	1*	57°W	72°W	4.0	0.45	8.9
	2	27°E	7°E	2.4	0.13	
	3*	38°W	42°W	2.6	0.57	4.6
	4	16°W	34°E	0.7	0.27	
50°N	1	41°W	6°W	4.7	0.39	
	2*	20°E	27°E	4.7	0.65	7.2
	3*	32°W	28°W	2.6	0.86	3.0
	4*	25°W	20°W	1.2	0.36	3.3
60°N	1	26°W	49°E	4.0	0.14	
	2*	13°E	10°E	5.0	0.97	5.2
	3	34°W	25°W	2.1	0.75	
	4*	25°W	27°W	0.9	0.25	3.6

* Indicates that the phase difference between the designated zonal harmonic component of $\bar{T}$ and $\nabla \cdot \overline{v'T'}$ is less than 0.05 cycle.

correspondence. This is particularly evident for zonal wavenumbers 2 and 3, for which the dissipative time scale is typically 3–7 days. Hence, in the absence of other dynamical processes, the strong departures from zonal symmetry of the mean temperature field, which is a measure of the available potential energy of the stationary waves, would be destroyed by the transient eddy heat fluxes within a matter of several days[10].

c. Other levels

The heat balances at the 850, 500 and 300 mb levels have also been diagnosed in an analogous manner. The results (not shown) indicate that the locations of the principal diabatic heating maxima and minima at different pressure levels are fairly coherent between 1000 and 300 mb. The magnitudes of these local maxima and minima generally decrease with height up to the 700 mb level, and are roughly uniform with height above that level.

Brown (1964) has computed the daily distributions of mid-tropospheric diabatic heating using the first law of thermodynamics, with vertical velocity deduced from the vorticity equation. The twice daily NMC analyses of geopotential height at 850 and 500 mb for selected months of the 1959–62 period were used in his study. The monthly averaged distribution of diabatic heating for the 800–400 mb layer in January 1962, as shown in Fig. 1a of his paper, is in qualitative

agreement with that displayed in Fig. 21 of the present study. Our heating distributions display a relatively stronger spatial coherence, probably due to the fact that the present data set covers a much more extended period.

Geller and Avery (1978) deduced the diabatic heating as a residue of the time-averaged thermodynamic energy equation. Their work made use of the circulation statistics documented by Oort and Rasmusson (1971). This set of statistics was derived from station data for the 1958–63 period. The time-averaged distributions
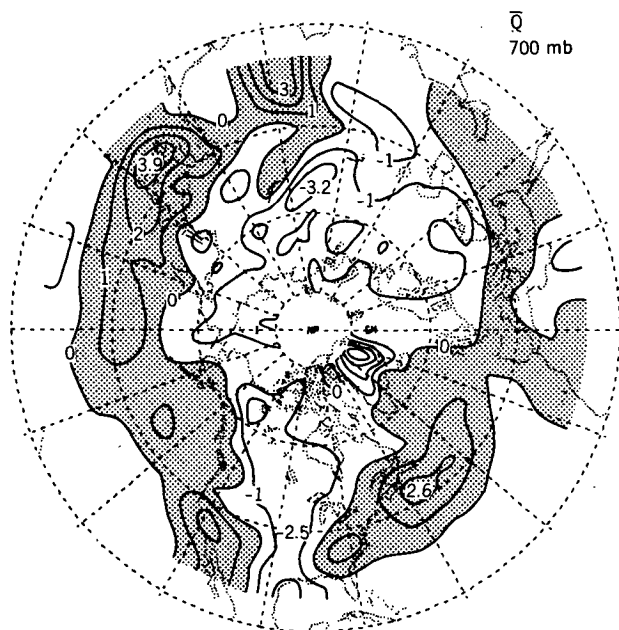

FIG. 21. Distribution of diabatic heating rate $\bar{Q}$ at 700 mb. Contour interval 1°C day^{-1}.

---

[10] Since the adiabatic heating and cooling associated with the time-averaged circulations induced locally by the transient disturbances may compensate the eddy heat flux convergence to a certain extent, the dissipative time scale corresponding to the net effect of the transient eddies may be longer than that presented in Table 1.

of vertical motion ($\bar{\omega}$) were calculated by the kinematic method, with the boundary conditions that $\bar{\omega}$ vanishes at the 1000 and 25 mb levels (see Oort and Rasmusson, 1971, Section 5A3). Geller and Avery also observed heating maxima over the Gulf Stream and the Kuroshio, and cooling over the interiors of the two continents. Their distributions indicate that the eastern oceans are characterized by cooling, whereas our results suggest that diabatic heating extends almost all the way across the Atlantic and the Pacific. Our study indicates that the strong divergence of heat fluxes by transient eddies over the southwestern United States and the adjacent oceanic areas (Fig. 20c) has to be balanced by diabatic heating over that region at 700 mb (Fig. 21). This feature is not observed by Geller and Avery. The intensity of the principal heat sources and sinks in our results tends to decrease with altitude between the 1000 and 700 mb levels, and remains almost uniform above 700 mb; whereas Geller and Avery's distributions indicate that the heating associated with the Kuroshio is much stronger at 500 mb than at 900 mb. In general, the heating patterns in our study exhibit a more distinct relationship to the distribution of continents and oceans, and to the major orographic features.

The gross features of our heating distributions are also similar to those presented by Hayashi and Golder (1977, Fig. 5.10) using data from a general circulation model.

8. Discussion

In the foregoing sections, a detailed account on the observed structure and the associated transport characteristics of tropospheric stationary waves has been given. The relative contributions of the stationary and transient motions to local, time-averaged budgets of vorticity and heat have been examined. The local advection of absolute vorticity by the time-averaged flow was found to be relatively stronger than the convergence of vorticity transports by transient eddies. It was then demonstrated that physically realistic hemispheric fields of time-averaged horizontal divergence and diabatic heating may be deduced as residuals in these balances. The distributions of the time-averaged divergence and heating fields are closely related to topographical features at the earth's surface.

The in-phase relationship between the divergence of transient eddy heat fluxes ($\nabla \cdot \overline{\mathbf{v}'T'}$) and the departure from zonal symmetry of the time averaged temperature field ($\bar{T}^*$) at 700 mb suggest that heat transports by transient eddies in middle latitudes constitute an efficient sink of available potential energy in the stationary waves. This dissipative mechanism acts on a time scale of about a week, which is comparable to the spin-down time associated with Ekman pumping (Holton, 1974, Chap. 6). The significance of this finding will be further examined in a forthcoming paper,

in which the results from a comprehensive study of the energy balance of the stationary waves are presented.

APPENDIX

Method of Solution of Eq. (2)

Eq. (2) may be rewritten as

$$\frac{\partial^2}{\partial \lambda^2}\bar{v}^* + \cos^2\phi \frac{\partial^2}{\partial \phi^2}\bar{v}^* + \frac{a \cos^2\phi}{[\bar{u}]}\frac{\partial}{\partial \phi}\bar{v}^*\frac{\partial}{\partial \phi}[\bar{\eta}] - 3\cos\phi \sin\phi\frac{\partial \bar{v}^*}{\partial \phi}$$

$$-\bar{v}^*(\cos^2\phi - \sin^2\phi) = -\frac{a^2 \cos^2\phi}{[\bar{u}]}\left\{[\bar{\eta}]\cdot\bar{D}_H^* + \frac{1}{a \cos\phi}\right.$$

$$\left. \times\left(\frac{\partial}{\partial \lambda}\overline{u'\zeta'} + \frac{\partial}{\partial \phi}\overline{v'\zeta'}\cos\phi\right)^*\right\}, \quad \text{(A1)}$$

where $\bar{v}^* = (1/a \cos\phi)\partial\bar{\psi}^*/\partial\lambda$ is the perturbation meridional velocity. By making use of the NCAR software subroutine SEPELI (NCAR, 1978), the fourth-order finite difference approximation to the separable elliptic equation expressed in (A1) is solved for $\bar{v}^*(\lambda,\phi)$ over the domain $0° \leqslant \lambda \leqslant 360°$ and $25° \leqslant \phi \leqslant 70°$ with the boundary conditions

$$\left.\begin{array}{l} \bar{v}^*(0°,\phi) = \bar{v}^*(360°,\phi) \\ \bar{v}^*(\lambda,70°) = \bar{v}^*_{\text{obs}}(\lambda,70°) \\ \bar{v}^*(\lambda,25°) = \bar{v}^*_{\text{obs}}(\lambda,25°) \end{array}\right\}, \quad \text{(A2)}$$

where $v_{\text{obs}}(\lambda,\phi)$ is the observed meridional velocity.

The perturbation zonal velocity $\bar{u}^*$ is computed from the continuity equation

$$\frac{1}{a \cos\phi}\left(\frac{\partial}{\partial \phi}\bar{v}^* \cos\phi + \frac{\partial \bar{u}^*}{\partial \lambda}\right) = 0. \quad \text{(A3)}$$

The NCAR software subroutine PWSSSP ·(NCAR, 1978) is then used to solve for the total streamfunction $\psi(\lambda,\phi)$ in the Poisson's equation

$$\nabla^2 \bar{\psi} = \bar{\zeta}, \tag{A4}$$

with the boundary conditions that $\bar{\psi}(\lambda,\phi) = \bar{\psi}_{obs}(\lambda,\phi)$ for $\phi = 25°$ and $70°$. Here

$$\bar{\zeta} = \frac{1}{a\cos\phi}\left\{ -\frac{\partial}{\partial\phi}([\bar{u}]+\bar{u}^*)\cos\phi + \frac{\partial\bar{v}^*}{\partial\lambda} \right\}$$

is the relative vorticity and $\bar{\psi}_{obs}(\lambda,\phi)$ the observed streamfunction.

REFERENCES

Berkofsky, L., and E. A. Bertoni, 1955: Mean topographic charts for the entire earth. *Bull. Amer. Meteor. Soc.*, 36, 350–354.

Blackmon, M. L., J. M. Wallace, N-C. Lau and S. L. Mullen, 1977: An observational study of the Northern Hemisphere wintertime circulation. *J. Atmos. Sci.*, 34, 1040–1053.

Bolin, B., 1950: On the influence of the earth's orography on the general character of the westerlies. *Tellus*, 2, 184–195.

Brown, J. A., 1964: A diagnostic study of tropospheric diabatic heating and the generation of available potential energy. *Tellus*, 16, 371–388.

Bunker, A. F., 1976: Energy exchange charts of the North Atlantic Ocean. *Bull. Amer. Meteor. Soc.*, 57, 670–678.

Burger, A. P., 1958: Scale consideration of planetary motions of the atmosphere. *Tellus*, 10, 195–205.

Charney, J. G., and A. Eliassen, 1949: A numerical method for predicting the perturbations of the middle latitude westerlies. *Tellus*, 1, 38–54.

Clapp, P. F., 1956: Some considerations involved in preparing long-range forecasts by numerical methods. *J. Meteor.*, 13, 341–350.

——, 1961: Normal heat sources and sinks in the lower troposphere in winter. *Mon. Wea. Rev.*, 89, 147–162.

Crutcher, H. L., 1959: *Upper Wind Statistics Charts of the Northern Hemisphere*, Vols. 1 and 2. NAVAER 50-1C-535, Office of the Chief of Naval Operations, Washington, D.C.

——, and J. M. Meserve, 1970: *Selected Level Heights, Temperatures and Dew Points for the Northern Hemisphere*. NAVAIR 50-1C-52 [U.S. Govt. Printing Office, Washington, D. C.].

Derome, J., and A. Wiin-Nielsen, 1971: The response of a middle-latitude model atmosphere to forcing by topography and stationary heat sources. *Mon. Wea. Rev.*, 99, 564–576.

Egger, J., 1976a: The linear response of a hemispheric two-level primitive equations model to forcing by topography. *Mon. Wea. Rev.*, 104, 351–364.

——, 1976b: On the theory of the steady perturbations in the troposphere. *Tellus*, 28, 381–390.

Geller, M. A., and S. K. Avery, 1978: Northern Hemisphere distribution of diabatic heating in the troposphere derived from general circulation data. *Mon. Wea. Rev.*, 106, 629–636.

Hayashi, Y., and D. G. Golder, 1977: Space-time spectral analysis of midlatitude disturbances appearing in a GFDL general circulation model. *J. Atmos. Sci.*, 34, 237–262.

Holopainen, E. O., 1970: An observational study of the energy balance of the stationary disturbances in the atmosphere. *Quart. J. Roy. Meteor. Soc.*, 96, 626–644.

——, 1978: On the dynamic forcing of the long-term mean flow by the large-scale Reynold's stresses in the atmosphere. *J. Atmos. Sci.*, 35, 1596–1604.

Holton, J. R., 1974: *An Introduction to Dynamic Meteorology*. Academic Press, 319 pp.

Kasahara, A., T. Sasamori and W. M. Washington, 1973: Simulated experiments with a 12-layer stratospheric global circulation model. I. Dynamical effect of the earth's orography and thermal influence of continentality. *J. Atmos. Sci.*, 30, 1229–1251.

Lau, N-C., 1978: On the three-dimensional structure of the observed transient eddy statistics of the Northern Hemisphere wintertime circulation. *J. Atmos. Sci.*, 35, 1900–1923.

——, 1979: The structure and energetics of transient disturbances in the Northern Hemisphere wintertime circulation. *J. Atmos. Sci.*, 36, 982–995.

Mak. M., 1978: On the observed momentum flux by standing eddies. *J. Atmos. Sci.*, 35, 340–346.

Manabe S., and J. L. Holloway, Jr., 1975: The seasonal variations of the hydrologic cycle as simulated by a global model of the atmosphere. *J. Geophys. Res.*, 80, 1617–1649.

——, and T. B. Terpstra, 1974: The effects of mountains on the general circulation of the atmosphere as identified by numerical experiments. *J. Atmos. Sci.*, 31, 3–42.

Molla, A. C., Jr., and C. J. Loisel, 1962: On the hemisphere correlations of vertical and meridional wind components. *Geofis. Pura Appl.*, 51, 166–170.

Möller, F., 1951: Quarterly charts of rainfall for the whole earth. *Petermanns Geograph. Mitt.*, 95, 1–7.

NCAR, 1978: NCAR software support library, Vol. 2. NCAR Tech. Note TN/IA-105.

O'Brien, J. J., 1970: Alternative solutions to the classical vertical velocity problem. *J. Appl. Meteor.*, 9, 197–203.

Oort, A. H., and E. M. Rasmusson, 1971: *Atmospheric Circulation Statistics*. NOAA Prof. Pap. 5, U.S. Dept. of Commerce, 323 pp.

Saltzman, B., 1965: On the theory of the winter-average perturbations in the troposphere and stratosphere. *Mon. Wea. Rev.*, 93, 195–211.

——, 1970: Large-scale atmospheric energetics in the wave-number domain. *Rev. Geophys. Space Phys.*, 8, 289–302.

——, and A. Fleisher, 1960a: The exchange of kinetic energy between larger scales of atmospheric motion. *Tellus*, 12, 374–377.

——, and ——, 1960b: The modes of release of available potential energy in the atmosphere. *J. Geophys. Res.*, 65, 1213–1222.

——, and M. Sankar Rao, 1963: A diagnostic study of the mean state of the atmosphere. *J. Atmos. Sci.*, 20, 438–447.

——, and F. E. Irsch, 1972: Note on the theory of topographically forced planetary waves in the atmosphere. *Mon. Wea. Rev.*, 100, 441–444.

Smagorinsky, J., 1953: The dynamical influence of large-scale heat sources and sinks on the quasi-stationary mean motions of the atmosphere. *Quart. J. Roy. Meteor. Soc.*, 79, 343–366.

U.S. Dept. of Commerce and U.S. Air Force, 1971: *Global Atlas of Relative Cloud Cover 1967–70*, p. 106 [National Climatic Center, Asheville, NC 28801].

van Loon, H., R. L. Jenne and K. Labitzke, 1973: Zonal harmonic standing waves. *J. Geophys. Res.*, 78, 4463–4471.

Wiin-Nielsen, A., J. A. Brown and M. Drake, 1963: On atmosphere energy conversions between the zonal flow and the eddies. *Tellus*, 15, 261–279.

——, —— and ——, 1964: Further studies of energy exchange between the zonal flow and the eddies. *Tellus*, 16, 168–180.